Clay-inspired MXene-based electrochemical devices and photo-electrocatalyst: State-of-the-Art progresses and challenges

By *Hou Wang, Yan Wu, Xingzhong Yuan, Guangming Zeng, Jin Zhou, Xin Wang,* Jia Wei Chew **

Dr. Hou Wang, Dr. Yan Wu, Prof. Xin Wang, Prof. Jia Wei Chew **
School of Chemical and Biomedical Engineering,
Nanyang Technological University,
Singapore 637459, Singapore.
*E-mail: jchew@ntu.edu.sg; wangxin@ntu.edu.sg

Prof. Xingzhong Yuan, Prof. Guangming Zeng,
College of Environmental Science and Engineering,
Hunan University,
Changsha 410082, P. R. China

Prof. Jin Zhou
School of Chemical Engineering
Shandong University of Technology,
Zibo 255049, P. R. China

Prof. Jia Wei Chew
Singapore Membrane Technology Center,
Nanyang Environment and Water Research Institute,
Nanyang Technological University,
Singapore 639798, Singapore

Keywords: MXene, supercapacitor, battery, photocatalyst, and electrocatalyst

MXene, an important and increasingly popular category of post-graphene two-dimensional (2D) nanomaterials, has been rigorously investigated since early 2011, because of advantages including flexible tunability in element composition, hydrophobicity, metallic nature, unique in-plane anisotropic structure, high charge-carrier mobility, tunable band-gap, and favorable optical and mechanical properties. To fully exploit these potentials and further expand beyond the existing boundaries, novel functional nanostructures spanning monolayer, multilayer, nanoparticles and composites have been developed by means of intercalation, delamination, functionalization, hybridization, among others. Undeniably, the cutting-edge developments and applications of clay-inspired 2D MXene platform as electrochemical electrode or photo-electrocatalyst have conferred superior performance and have made significant impact in the field of energy and advanced catalysis. This review provides an overview in the fundamental properties and synthesis routes of pure MXene, functionalized MXene and their hybrids, highlights the state-of-the-art progresses of MXene-based applications with respect to supercapacitors, batteries, electrocatalysis and photocatalysis, and presents the challenges and prospects in the burgeoning field.

1. Introduction

The escalating global energy consumption has accelerated the development of means for energy production. Green and renewable energy technologies including supercapacitors, batteries, electrocatalysis and photocatalysis are urgently needed to enhance sustainability and reduce adverse environmental impact.[1-3] New material structures and properties are promising for further augmenting the performance of these technologies. Two-dimensional (2D) nanomaterials have tremendous impact on both fundamental studies and practical applications in numerous fields.[4-7] Since the discovery of graphene led to a Nobel Prize in Physics in 2010, such ultrathin films has become enthralled materials heralding a new generation of state-of-the-art devices.[8] Most importantly, the ground-breaking discovery and successful applications of graphene has inspired the rapid development of atomically thin 2D materials beyond graphene, including the single-element materials (e.g., silicene,[9] germanene, [10] phosphorene[11] and borophene[12]), the more popular two-element materials (e.g., hexagonal boron nitride (h-BN),[13, 14] transition metal dichalcogenides (TMDs) and oxides,[15, 16] carbon nitride,[17] and the multi-element ones (e.g., layered metal hydroxides,[18] clays,[19] metal organic frameworks and covalent organic frameworks) [20].

MXene, the generic term for transition metal carbides/carbonitrides/nitrides, is the latest and represents an important group of layer-structure materials that is characteristic of metal-carbon and/or nitrogen host layer with/without functional groups in the surface termination.[21, 22] It can be divided into two categories, namely, one with the structural formula of $M_{n+1}X_n$ and the other $M_{n+1}X_nT_x$, whereby M is a transition metal (i.e., Sc, Ti, V, Cr, Zr, Hf, Nb, Mo, Ta and W), X is carbon and/or nitrogen, T_x is the terminated functional groups (i.e. -OH, -O or -F), and n is an integer typically between 1-3. The M atoms are arranged in hexagonal close packing with the X atoms sitting in their octahedral interstice. Taking n = 2 as an example (Figure 1a), M_3X_2 is such that three M layers are interspersed alternately with two X layers in an $[MX]_2M$ arrangement.[23] The atoms sit in a covalently bonded layer with three M and two X atomic layers arranged alternately, forming an edge-shared M_6X octahedra.[24] This kind of unique structure is derived from the original bulk $M_{n+1}AX_n$ phase by selectively separating the most reactive fraction (namely, A, which is a

group IIIA or IVA element).[24] There is generally a coordination number of six for a transition metal ion, therefore making six chemical bonds with the neighboring X atoms and the attached chemical groups on the surface form $M_{n+1}X_nT_x$.[25] Thereby, an extremely large set of properties for MXene can be generated by the different combinations of components, the numbers of MX layers between the fraction of A and the change of surface termination group chemistry.

Notably, MXene with hexagonal lattice symmetry and metallic nature has exhibited many unique properties in terms of excellent metallic conductivity (or transition phase), tunable band gap structure, anisotropic behavior of carrier mobility (~74100 cm^{-2} V^{-1} s^{-1} and ~22500 cm^{-2} V^{-1} s^{-1} along different directions) at room temperature, layer-dependent optical transparency and absorption, good Young's modulus (~502 GPa), and good thermal conductivity and transformation.[26-31] It is worth noting that, with respect to the manipulation of structure and property, reliable synthetic routes have been preliminarily developed to prepare pure MXene and their composites, including acid etch and its auxiliary methods,[32, 33] chemical vapour deposition,[34, 35] chemical reduction,[36] (solvo)hydrothermal method,[37] calcination, [38] and so on. They have also been tailored to fulfill the requirement for practical applications, including energy conversion and storage,[39, 40] catalysis,[41] adsorption,[42-44] membrane separation,[45] sensor,[46] field effect transistors,[47] photothermal conversion,[48, 49] and cellular imaging [50]. The number of publications on MXene, according to ISI Web of Science, has increased exponentially since the pioneering studies reported by Naguib et al. [33] from 4 papers in 2011 to 133 papers in 2016. More than 102 papers have been published since the start of 2017 till August 8, 2017.

Undoubtedly, the research about MXene is still at its infancy stage. Their properties are still poorly understood and more potentials are largely unexploited. The important implications of this burgeoning 2D material necessitate timely reviews of the state-of-the-art developments to streamline efforts. Although several excellent reviews on various MXene-based fields (e.g., theoretical analysis, energy storage, MXene thin-film, electrochemical capacitor electrodes, etc.) have sprouted, [21, 22, 25, 51-53] a thorough summary and assessment on the recent breakthroughs on electrochemical devices remains a gap in the

knowledge base. Therefore, this review focuses on Mxene from the perspective of electrochemical devices and photo/electrocatalysts, in particular with respect to the unique traits of MXene materials in the realm of 2D materials, the comparisons of synthetic strategies, and the advances of photo-electrocatalysis. The present review begins with an overall description of the unique traits and properties of MXene, then discusses the synthesis and characterization of pure MXene, functionalized MXene and their hybrids, and highlights the state-of-the-art progresses with respect to supercapacitors, batteries, electrocatalysis and photocatalysis. The challenges and prospects for future development of these fields are finally outlined. This review is expected to be valuable to the international research communities from wide-ranging disciplines, including material science, chemistry and engineering.

2. The unique traits and properties of MXene

In the world of 2D materials beyond graphene, several materials such as graphdiyne, transition metal dichalcogenides (TMDs), layered perovskite, *h*-boron nitride, borophenes, silicene, carbon nitride and black phosphorus, have been widely studied in the energy and catalysis field.[7, 20] As a comparison, several outstanding characteristics regarding the compositions and structures of MXene are highlighted as follows. As shown in Figure 2, at the atomic scale, a wide variety of metal elements (Sc, Ti, Zr, Hf, V, Nb, Ta, Cr, Mo, Mn, etc) can be chosen to construct stable MXene with various composition (single, double or ternary) as well as proportion and arrangement.[22, 54] This feature offers many basic prerequisites for regulating metallic conduction and active sites, and also is promising for the application of MXene-based materials in advanced catalysis and energy area. Secondly, at the mesoscopic level, one of the most important features of MXene is the surface termination groups, such as -F, -O and -OH.[55] The exposed groups in MXene make them more feasible as heterogeneous catalysts range from metallic to semiconducting and also act as possible anchor sites for further modifications with other molecules or nanostructures. Thirdly, under certain conditions like heat treatment at oxidative atmosphere, MXene tends to convert into other compounds, such as TiO_2, amorphous carbon and even graphene quantum dots,[56, 57] and thus can be utilized as universal precursors to produce many ultrathin materials such as metal

oxides, metal-carbon hybrids and graphene-functionalized hybrids.

MXene has numerous different kinds of properties, which play important roles in the performance of electrochemical devices and photo-electrocatalysts. The different applications are underlain by the electronic, transport and band gap properties. Moreover, the layer structure, thermal and mechanical properties also could make a significant difference. For example, as the LIB anode materials, MXene has excellent electronic conductivity, low operating voltage range of -0.2 to 0.6 V vs. Li/Li^+, low diffusion barriers (due to the terminated groups) which are favorable for high rate performance and exceptional mechanical properties that are invariant to Li adsorption.[55] In the field of MXene-based electrodes supercapacitor, the layer $Ti_3C_2T_x$ structure can produce electrolyte ions intercalation-induced capacitance.[58] The valence alteration of transition metal (such as the Ti oxidation state) may also contribute to the pseudo-capacitance. For the MXene (M_2CT_x, M = Ti, Zr, and Hf) in photocatalysis applications, the band gap in the range of 0.92–1.75 eV shows very good light absorbance at wavelengths from 300 to 500 nm.[59,60] Meanwhile, the large and anisotropic carrier (electron and hole) mobility in MXene systems facilitates the migration and separation of photogenerated electron–hole pairs, making them promising for photocatalytic hydrogen generation and pollutant degradation. For electrocatalysis, MXene usually are used as the supporting materials, which may alter the electrophilicity of the active centers of the catalysts. This may hinge on the ultralow work function, electrical conductivity and electronegative surfaces of MXene.[61,62]

Electronic, transport and band gap properties One of the most important properties of MXene is the metallic behavior with a substantial electron density near the Fermi level.[63] The metallic conductor properties can be not only regulated by the formation of additional Ti-X bonds, but also changed to narrower band-gap semiconductor by adjusting the species and orientations of the surface termination on MXene.[53-65] For example, the monolayer Ti_2CO_2 semiconductor with a band gap of 0.91 eV displayed strongly anisotropic behavior with the estimated electron mobility of 611 $cm^{-2}\ V^{-1}\ s^{-1}$ and 254 $cm^{-2}\ V^{-1}\ s^{-1}$ along respectively the x and y directions, while the hole mobility of 74100 $cm^{-2}\ V^{-1}\ s^{-1}$ and 22500 $cm^{-2}\ V^{-1}\ s^{-1}$ was obtained along respectively the x and y directions under ambient temperature

condition.[26] Similar anisotropic carrier transfer has been shown in Sc_2CF_2 with values of 5.03×10^3 and 1.07×10^3 cm^{-2} V^{-1} s^{-1} in the zigzag and armchair directions, respectively.[68] It had also been estimated that the density of free carriers for freestanding $Ti_3C_2T_x$ monolayers was $8\pm3\times10^{21}$ cm^{-3}.[69] The electrical conductivity of the $Ti_3C_2T_x$ flake was measured to be 4600±1100 S cm^{-1} and the field-effect electron mobility was 2.6 ± 0.7 cm^{-2} V^{-1} s^{-1}.[70, 71] The resistivity of multilayer $Ti_3C_2T_x$ films was one order-of-magnitude higher than the resistivity of individual flakes, which surpassed even the stack 2D graphene sheet, and was due to the contact resistances at the interfaces between individual MXene flakes (i.e., the resistance perpendicular to the basal plane). Increasing the heat treatment temperature to 600 °C could further increase the conductivity of Ti_3C_2 from 850 S cm^{-1} to 2410 S cm^{-1}, because of the decrease of surface functional groups and the formation of short conduction paths.[72] Moreover, by controlling the Ti vacancy concentration in $Ti_3C_2T_x$, the measured conductivity of single-layer $Ti_3C_2T_x$ was up to 6.76×10^5 S m^{-1}, which was comparable with graphene (6×10^6 S m^{-1}) and MoS_2 (8×10^3 S m^{-1}), since the defective –OH terminated single-layer Ti_3C_2 was still metallic with no change in the density of state.[73] Attributing to the higher unfilled *p* orbitals of O compared to OH, the *n*-type systems of transition metal (TM) doped $Sc_2C(OH)_2$ semiconductors could be changed to the *p*-type systems for the TM-doped Sc_2CO_2.[74] Moreover, the band gap modulation of Sc_2CO_2 bilayers, dominated by the interlayer *van der Waals* and electrostatic interactions, has been shown to be dependent on the relative stacking position and distance, as well as the magnitude and direction of external electric field.[75] Recent research has indicated that the conductivity and transport of MXene can be adjusted via plasma treatment, or by introducing conductive materials like graphene for the modification of terminated groups in order to form a cross-linked and electrically conducting network.[23, 76, 77]

Band gap, another important electronic property, can be engineered by surface termination modification, metal atom substitution, strain modulation and hybridization.[78-83] It has been experimentally demonstrated that the surface groups of Ti_2CT_x can adjust the band gap of the Ti_2C layer without affecting the basic framework.[78] The dominant charge transport of activated carriers over the narrow energy gaps of the transition metal carbides leads to less

sensitivity to the measured transport gap for field-effect mobility at room temperature. Strain engineering is the other mode to modulate the band gap properties. For monolayer Sc_2CO_2, after more than 2% tensile strain, the normal Γ (valence band maximum) to K (conduction band minimum) indirect band gap of 1.82 eV would turn into the Γ to K direct band gap of 1.39 eV. This has been verified by the variations of the band gap properties being the out-of-plane orbital in the Sc_A (O_B) atoms at the Γ (K) point of the valence band and the in-plane orbital in the Sc_A atom at the K point of the conduction band.[80] A similar transition from indirect to direct band has also been demonstrated under biaxial or uniaxial strain with 4%, 14% and 10% for monolayer Ti_2CO_2, Hf_2CO_2, and Zr_2CO_2, respectively.[81] In addition, the ordered single-transition-metal $M_3X_2T_x$ like $Ti_3C_2T_x$ is usually metallic while the double-transition-metal $M_2'M''X_2T_x$ (where M' and M'' are two different transition metals, such as Mo, Cr, Mn, Hf, V or Ti) exhibits semiconductor-like transport behavior.[84,85] For example, the $Hf_2MnC_2T_x$ and $Hf_2VC_2T_x$ monolayers were ferromagnetic semiconductors in their ground state. Substituting Mo for Ti in $Ti_3C_2O_2$ could induce the metallic-semiconducting translation for $Mo_2TiC_2O_2$ due to the chemical bonding (O2p–Mo2-4d, C2p–Mo2-4d and C2p–Ti1-3d) and the electronic coupling of oxygen and carbon with metals (O-Mo).[79] The split effect of spin-orbit coupling splits the $d_{x^2-y^2}$ and d_{xy} of the Mo atom, which degenerates at Γ-point and opens a tiny gap (0.04 eV), generating an indirect band gap of 0.17 eV. Broadly speaking, these excellent electronic, transport and band gap properties make MXene-based materials feasible in electrochemical electrode and catalyst applications.

Optical properties It is generally acknowledged that the absorption edge approaches zero due to the metallic nature of MXene.[41] However, interband transitions (IBT) involving the surface Ti dz^2 orbitals hybridized with C *p* states has a prominent effect on the dielectric response (i.e., $\varepsilon_{2,xx}$ (**0**,ω)), affecting the optical properties of the multilayer Ti_3C_2. Valence electron energy-loss (VEEL) spectroscopy showed that the interband transition was very sensitive to the T_x groups localization on the MXene surface and induced a 40% variation of optical conductivity in the middle of the visible spectrum.[86] In this respect, the surface functionalization (or functional groups) increased the absorption of MXene to the visible light

range.[87] From the first-principles density functional theory calculations, compared with pristine Ti_3C_2, both fluorinated and hydroxylated $Ti_3C_2T_2$ enhanced ultraviolet absorption and reflectivity, and both properties were also improved by the surface oxidation in the visible light range.[88] It has been verified that the $Ti_3C_2T_2$ film could absorb light in the UV-Vis region from 300 to 500 nm and also exhibit a broad absorption band at around 700–800 nm, depending on the thicknesses of film.[89] Transmittances of 91.2% and 43.8% can be obtained for thicknesses of 5 nm and 70 nm, respectively. Interestingly, the conductive $Ti_3C_2T_x$ spincast films, synthesized by water-based solution-processing steps, were plasmonic materials and had free-electron plasma oscillations above 1130 nm.[90] Moreover, the optical properties of MXene can be regulated via incorporating with the other components including blue phosphorene, metal sulfide or TiO_{2-x}.[41, 91, 92] For example, pure Zr_2CO_2 exhibited favorable optical absorption performance approximately in the range of 300 to 500 nm.[91] After stacking the blue phosphorene in terms of van der Waals heterostructure, the optical absorption had a red shift towards the visible light region under the biaxial compressive strain due to the band gap variations of Zr_2CO_2 under deformation. Collectively, these optical properties favor the development of MXene in photocatalytic, photovoltaic, and transparent conductive electrode devices.

Mechanical properties A higher electron density within the $M_{n+1}X_n$ layers causes the apparent difference between monolayer 2D materials and their bulk counterpart. The intrinsic mechanical properties of free-standing mono-layer Ti_3C_2 have been predicted, with the in-plane Young's modulus being as high as 502 GPa.[28] Under biaxial strains, the elastic modulus of Mo_2C was calculated to be 312 ± 10 GPa, surpassing that of monolayer MoS_2 because of the strong interactions between molybdenum and carbon atoms, and the ideal strength was determined to be 20.8 GPa at a critical strain of 0.086.[29] The breaking strength of pristine MXene (M = Sc, Mo, Ti, Zr, Hf. X = C, N. n = 1) has been predicted to be between 92 and 161 N m^{-1},[93] which implies favorable mechanical stability. 2D Ti_2C is an elastically isotopic 2D material with different mechanical properties in the zigzag direction (x direction) and the armchair direction (y direction), with the corresponding Young's modulus E_x and E_y being 620 GPa and 600 GPa, respectively.[94] Due to the stretch and shrinkage of Ti–C bonds

before and after the critical strains, pure 2D Ti_2C could sustain strains of 9.5%, 18% and 17% under biaxial tension, uniaxial tension along the x direction, and uniaxial tension along the y directions, respectively. After functionalizing the surface with oxygen, the strains of 2D Ti_2CO_2 increased to 20%, 28% and 26.5%, caused by the slow down in the collapse of the surface atomic layer because of strong covalent bonds between the Ti atom and the surface terminal groups.[94] Bonding strength (or coupling interaction) is the key factor for maintaining the elastic stiffness.[95] Attributed to the van der Waals and hydrogen bonds between the sheets, the gap distance between two $Ti_3C_2T_x$ layers was only 0.57 Å for OH termination, which was much narrower than ~2.5 Å for O and F termination. Thus, there was more advantageous normal-to-the-plane elastic modulus for the Ti_3C_2 decorated with OH group.[96] Characterized by the contact resonance atomic force microscopy, the elastic modulus of flat $Ti_3C_2T_x$ flake was found to range from 12 to 75 GPa in air, and from 7 to 70 GPa in water.[96] Moreover, the mechanical property of $Ti_3C_2T_x$ films could be reinforced by polymers like chitosan and polyethylene.[97, 98] The introduction of chitosan could expand the displacement of $Ti_3C_2T_x$ nanosheets and increase the tensile strength of films continuously from 8.20 to 43.52 MPa.[98]

Thermal properties The thermal conductivity of Ti_2CO_2, Zr_2CO_2, Hf_2CO_2 and Sc_2CF_2 at room temperature in the armchair direction are reported to be 23, 62, 86 and 472 Wm^{-1} K^{-1}, respectively, depending on the length of the measured MXene flake. The thermal conductivity of Sc_2CF_2 increased to 722 W m^{-1} K^{-1} with a 50 μm flake length and that of Hf_2CO_2 could reach 131.2 Wm^{-1} K^{-1} with a flake length of 100 μm, which were higher than that of pure iron, MoS_2 and phosphorene.[99, 100] The thermal expansion coefficient of Hf_2CO_2 was 6.094 $\times 10^{-6}$ K^{-1}.[99] It has been predicted that introducing the *n*-type dopant had enhanced the thermal conductivity of single-layer Mo_2C from 48.4 to 92.2 W m^{-1} K^{-1} at 500 K.[29] These satisfactory heat conduction and structural stability for MXene at certain temperatures are beneficial for the electronic and heat transformation devices.

The thermal stability of MXene also depends on their composition and the environment (e.g., air). Unsaturated Ti 3d orbitals of the pristine Ti_2C surface can interact strongly with O_2 molecules, leading to barrier-less O_2 dissociation to generate Ti_2CO_2 with O saturation.[101]

The resulting Ti_2CO_2 could repel O_2 and had thermodynamic stability at 550 °C. However, with a large portion of exposed metal atoms on the surface, part of the MXene were usually thermodynamically metastable with high surface energy, thereby suffering poor oxygen resistance in air.[102] From the thermo-gravimetric analysis, the $Ti_3C_2T_x$ (T_x = F or OH) was stable at temperatures of up to 800 °C in argon (Ar) atmosphere. On the contrary, it could be oxidized into anatase TiO_2 nano-crystals partly at 200 °C and fully transformed into rutile TiO_2, CO_2 and H_2O at 1000 °C in oxygen atmosphere.[103]

During the heat treatment process, the transformation twinning of Ti_2C nanosheets can be induced due to the existence of stacking faults,[104] but the nanoscale defects (i.e. vacancies, dislocations) can be eliminated without damage to the layered structure and hexagonal crystal structure of Ti_3C_2 at the stable phase at 1200 °C in Ar atmosphere.[56] Based on Raman and *in situ* TEM analysis, $Ti_3C_2T_x$ can be converted into carbon sheet-supported TiO_2 of different crystal structures, particle sizes and morphologies with the control of temperature, heating rate and oxidation time.[105] Those properties make MXene a viable support or template for synthesizing MXene-based hybrids or derivatives.

3. An overview of synthesis and characterization for pure MXene and their hybrids

To date, tremendous efforts have been made to develop synthetic methods for pure MXene and their derivatives. Intuitively, the synthesis route adopted would influence the surface chemistries of MXene and consequentially the function or behavior. To fully exploit the advantages of MXene, especially in various composites, it is important to know the synthesis, mechanism and characterization. Accordingly, the following section sheds light on these for pure MXene and MXene-based composites.

Pure MXene Although the metallic nature of M-X bonds make the mechanical separation of the $M_{n+1}X_n$ layers extremely difficult, the M-X bond exhibits lower chemical activity than that of the M-A bond, possibly causing the selective removal of the A element layers. Since the first synthesis of multi-layered $Ti_3C_2T_x$ by Naguib et al. [30] based on the top-down strategy through the selective etching of M-A bond by hydrofluoric acid (HF) at room temperature, the fluoride-based compounds (LiF, $NaHF_2$, KHF_2, NH_4HF_2 and molten fluoride salt) have been

developed to effectively prepare MXene.[27, 33, 107-109] The facile and simple strategy is suitable for the high-yield and easily scalable production of MXene. For the Al-containing MAX phase, general procedures can be summarized in Figure 1. The transformation of MAX to MXene with different shape, size and morphology is related to the HF concentration, the source of MAX, the reaction time and temperature, the delamination or intercalation agent (dimethyl sulfoxide, $NH_3 \cdot H_2O$ and urea), the washing solution and the drying methods.[101, 105, 110, 111] By replacing strong corrosive HF by bifluorides like KHF_2 or NH_4HF_2 as the etch agent, the etching and intercalation of Ti_3AlC_2 could be simultaneously occurring at 60 °C and the cation (e.g. K^+, NH_4^+) could enlarge the interplanar space of Ti_3C_2.[107] Using LiF and hydrochloric acid as the etchant without sonication, Lipatov et al.[70] adjusted the molar ratio of LiF to Ti_3AlC_2 to 7.5:1, resulting in monolayer $Ti_3C_2T_x$ flakes with a thickness of 1.5 nm with less defects (Figure 3a,b). The $Ti_3C_2T_x$ flakes with larger size of 4~15 μm had uniform and defect-free surfaces, and less ordered stacks. A facile hydrothermal way was proposed for the preparation of $Ti_3C_2T_x$ using NH_4F at 150 °C.[112] During this process, NH_4F would be hydrolyzed gradually to generate HF, which served as the etch agent to form $Ti_3C_2T_x$. Different kinds of etchant affect the surface termination group species of MXene. Nuclear magnetic resonance (NMR) spectroscopy verified that there were much more –OH and –F termination and fewer –O terminations in the HF synthesis sample, while a higher content of O-terminated titanium atoms were shown in contrast to –OH and –F terminal groups in LiF–HCl etched samples (Figure 3c,d).[113] X-ray photoelectron spectroscopy and X-ray absorption near edge structure analysis showed that the distribution of terminations was related to the various layer number, n value, and X element species.[114]

Some raw MAX phase, like bare ternary Hf-Al-C composite, cannot be selectively etched into Hf-containing MXene in HF solutions. *In situ* reactive pulsed electric current sintering process was firstly reported to replace the Al atoms in $Hf_3Al_4C_6$ with Si atoms, and then etch the $Hf_3[Al(Si)]_4C_6$ compound in HF solution to form lamellar $Hf_3C_2T_z$ with a thickness of ~2 nm and O-, F-containing surface termination (Figure 3e).[115] A substitutional solution of Si on the top Al sites effectively reduced the interfacial adhesion energy from 0.442 eV $Å^2$ to 0.211 eV $Å^2$ between Hf−C and Al(Si)−C sublayers within the unit cell of the parent

compound. The addition of larger atomic charge of silicon (2.36), compared to that of aluminum (2.19), caused the decrease of atomic charges of the Hf and C atoms and the weakness of the bond strength, thereby further facilitating the subsequent selective etching. Similar methods in the presence of HF or LiF + HCl etchant have also been applied to etch non-Al containing MAX phase for the synthesis of other MXene.[116, 119, 120] Using predesigned and in-plane chemical ordering $(Mo_{2/3}Sc_{1/3})_2AlC$ laminates as the raw quaternary MAX phase, 2D $Mo_{1.33}C$ sheets with ordered metal divacancies and outstanding electrical conductivities have successfully been obtained via selectively etching the Al and Sc atoms.[117] After HF etching and butylammonium hydroxide intercalation, monolayer $Mo_{1.33}C$ flakes with lateral dimensions of >1 μm had been obtained. The high-angle annular dark field scanning transmission electron microscopy (HAADF-STEM) showed a hexagonal-based crystal with chain-like features due to the presence of divacancies (Figure 3f). The undulating Mo-atomic chains were separated by ~4.7 Å and the projected interatomic distance was ~1.9 Å. In general, for top-down approaches, etching agents like corrosive fluoride and strong acid are usually used, which are difficult to dispose, and MXene flakes with significant amounts of defective and nanoporous/pitted structures may be generated during the synthesis process. In the primary stage, much more efforts should be channeled towards discovering new routes to prepare the existing or new kinds of MXene.

Developing a controlled approach for tailoring the morphology of MXene sheets would be a valuable strategy for controlling their functionality and properties. Without the assistance of any templates, 2D flat $Ti_3C_2T_x$ nanosheets could convert to 3D crumpled structure via a spray drying method (Figure 3g).[32] After etching, delamination and dispersion of $Ti_3C_2T_x$ nanosheets, $Ti_3C_2T_x$ dispersion was aerosolized at an aspirator pressure of 60 psi and dried using in-house air as a carrier gas at 220 ˚C. The capillary forces on the evaporating droplets induced the scroll, bend and fold of $Ti_3C_2T_x$ nanosheets for the formation of 3D crumpled structures. Excessive $Ti_3C_2T_x$ nanosheets had a more effective bending modulus, which facilitated the crumpling of the nanosheets and a less compact structure. Interestingly, this morphological change was reversible upon rehydration because of the few permanent defects or covalent bonds and the hydrophilic terminal groups. Unfortunately, this process could

cause the oxidation of titanium to TiO_2. To solve this disadvantage, it has recently demonstrated the selective synthesis of various Ti_2C morphologies using the selective intercalation of surfactant agent, *p*-phosphonic calix[*n*]arenes, into Ti_2C with the aid of ultrasonication.[117] The ring size of macrocycle in *p*-phosphonic acid calix[n]arene (PCX_n) defined the plates, crumpled sheets, spheres and scrolls of Ti_2C with n = 4, 5, 6, or 8 (Figure 3h). The mechanism of evolutionary morphology depended on the covalent bonding between the Ti_2C and the phosphonic acid moieties of calixarene, and the conformational flexibility and dexterity of phosphonic acid calixarene. Moreover, the template approach is attractive to produce well-defined architectures. Poly(methyl methacrylate) (PMMA) spheres had been used as the templates to integrate flakes via surface hydroxyl groups interaction.[120] The stable and well-dispersed hollow $Ti_3C_2T_x$ spheres formed after PMMA was removed through thermal evaporation at 450 °C.

Surface modification, involved in functional intercalant molecules, can alter the surface chemistry of MXene (e.g., Ti_2CT_x) so as to modulate the interlayer distance, ions diffusion and hydrophilicity/hydrophobicity.[76, 78, 121-125] For example, after etching the aluminum layers and replacing the surface groups (-OH, -F) of Ti_3AlC_2 powder in 40% HF solutions at room temperature, the Ti_3C_2 was alkalized in LiOH solution and subsequently immobilized the Sn^{4+} ion in polyvinylpyrrolidone (PVP)-contained $SnCl_4$ solution resulting in the PVP-Sn(IV)@Ti_3C_2 nanocomposite via ion-exchange and electrostatic interaction.[126] The PVP made for the dispersion and size control of nanoparticles. Similarly, immersing the Ti_3C_2 into cationic surfactant (hexadecyltrimethylammonium bromide, CTAB) solution had obtained a prepillared structure and subsequently reacted with Sn^{4+} to form CTAB-Sn(IV)@Ti_3C_2 pillared nanostructures.[125] Sulfanilic acid diazonium salts had grafted the phenyl-sulfonic groups and aryl groups onto the surface of Ti_3C_2 to produce stable colloidal dispersions of delaminating Ti_3C_2 flakes.[123] The negatively charged units on Ti_3C_2 surfaces combined with the presence aryl groups weakened the bonds between the MX layers, facilitating the delamination of the multi-layered MX structures. With the aid of -OH groups, the $Ti_3C_2T_x$ surface was functionalized by organofunctional siloxanes such as (3-Aminopropyl) triethoxysilane, (dodecyl) triethoxysilane, (methyl aniline) triethoxysilane, and

(c-methacryloxypropyl) trimethoxysilane in the mixture of ethanol, water and ammonium.[124] Four functional groups on $Ti_3C_2T_x$, namely -NH_2, -COOR, -C_6H_6, and -$C_{12}H_{26}$, can tune the hydrophilic/hydrophobic nature and the affinity towards solvent molecules like isopropanol, ethyl acetate, toluene, and *n*-heptane.

Other than the top-down synthesis strategies, bottom-up routes like chemical vapour deposition (CVD) has sprouted for the preparation of ultrathin Mo_2C, WC and TaC crystals.[34, 35, 127] Compared with the top-down synthesis, this strategy can produce large lateral sizes of high-quality MXene crystals with extremely low defect, disorder and impurity. For example, 2D ultrathin α-Mo_2C crystals with a uniform thickness of less than 3 nm and lateral sizes of over ~100 μm were synthesized at temperatures above 1085°C using methane as a carbon source and a Cu foil sitting on a Mo foil as the substrate. It had been reported that the α-Mo_2C had superior crystallinity with no defects or disorder. Using molten Mo–Cu alloy catalyst in CVD process, well-faceted Mo_2C single crystals with the widths of 50 μm~100μm and the thickness of ~8 nm could vertically grow onto graphene.[127] Graphene could passivate the catalyst surface and prevent the Mo atoms from reacting with methane, resulting in a change of grown ways from precipitation-limited to diffusion-limited process. However, bottom-up approaches have numerous disadvantages including tedious synthesis protocols and low-efficiency production. Inspired by the early acquisition, bottom-up strategies like plasma enhanced CVD with different metal substrates for the synthesis of high-quality MXene are expected to continue to advance.

MXene-inorganic nanostructure composites In order to enhance photoelectrochemical performance of MXene, quite a few inorganic nanostructure composites with integrated properties have been developed, which include metals like Pt, Ag, Rh, Au, Pd, Co and Ru,[36, 128-133] metal oxides like TiO_2, Cu_2O, Co_3O_4, Fe_2O_3, MnO_2, Nb_2O_5, MoO_3, ZnO, SnO_2, and NiO,[37, 38, 40, 44, 92, 134-144] and metal hydroxide[145] and chalcogenides like MoS_2 and CdS.[41, 146, 147] The fabrication methods are generally classified as chemical reduction, calcination and (hydro-) solvothermal preparation.

Chemical reduction is a fashionable strategy for synthesizing MXene-based metal composites. Precursor of metals, such as $AgNO_3$, $RhCl_3$, $RuCl_3$ and $CoCl_2$, can be simply

made *in situ*, reduced by ammonia borane, dimethyl sulfoxide, $NaBH_4$ and $Ti_3C_2T_x$. For example, Ag nanoparticles/$Ti_3C_2(OH)_{0.8}F_{1.2}$ composites was obtained by the direct self-reduction of $AgNO_3$ with $Ti_3C_2(OH)_{0.8}F_{1.2}$ due to the strong reductive activity on the low-valence Ti(II) and Ti(III) species.[36] To obtain anisotropic nanostructure, Ti_3C_2 was alkalized in NaOH solution and then treated by poly(vinylpyrrolidone) to construct $Ti_3C_2(OH/ONa)_2$.[131] After the injection of Ag ions, various Ag particle morphologies including dot-like nanotwin, nanowires and snow-shaped dendrite nanostructure formed with different reaction durations. Using the hydroxyl and carboxyl of alkalizing-$Ti_3C_2X_2$ as anchor sites, the Rh^{3+} ions were captured on the surface through coordination interaction and *in situ* reduction to Rh nanoparticles in the presence of $NaBH_4$ as reducing agent.[132]

The structure of MXene crystallites is significantly dependent on calcination temperatures because of the vulnerable resistance to oxidization. Thermal treatment of MXene at relatively high temperature promotes the phase transformation from thermodynamically metastable MXene to more stable and condensed transition metal oxides composites. It has been used to synthesize *in situ* layered orthorhombic Nb_2O_5@$Nb_4C_3T_x$ hierarchical composite *via* heating the $Nb_4C_3T_x$ (or Nb_2CT_x) in flowing CO_2 at 850 °C.[38] In the presence of CO_2, the external or interior layers of $Nb_4C_3T_x$ can be oxidized to orthorhombic Nb_2O_5 with interconnection to the $Nb_4C_3T_x$ by the disordered carbon "binder". After the liquid phase precipitation reaction on the surface or interlayer of Ti_3C_2 using $Mn(NO_3)_2$ and $KMnO_4$ as the precursor, the MnO_2/Ti_3C_2 nanocomposite can be synthesized by calcining at 300 °C in N_2 atmosphere.[139] Similar processes had also been used for the binary ZnO nanoparticles/Ti_3C_2 hybridization.[143] It had recently demonstrated that Ti_3C_2/TiO_2/CuO ternary nanocomposite could be prepared using cupric nitrate decomposition to CuO formation on the surface of Ti_3C_2 at 500 °C under an argon atmosphere.[148] Part of Ti_3C_2 was thermal-transformed into TiO_2.

The (hydro-)solvothermal method is a powerful tool for the preparation of MXene-based inorganic nanocrystals with high crystallinity without post-treated calcination. As an example, Cu_2O nanoparticles had been hybridized with titanium carbide by the reaction of $Cu(CH_3COO)_2{\cdot}H_2O$ and Ti_2CT_x powders in N,N-dimethylformamide (DMF) solution at 150 °C for 10 h.[37] The DMF acted as an intercalant and a weak reducing agent, causing the

formation of Cu_2O with the diameter of ~200 nm. Combining the hydrothermal oxidation route with hydrazine hydrate reduction, the TiO_{2-x}/Ti_3C_2 nanocomposite had been synthesized.[92] Using NH_4F as a facet controlling agent, Ti_3C_2 was prior oxidized into rutile TiO_2 octahedrons exposing active (111) facets. After N_2H_4 reduction at 200 °C, a large amount of bulk Ti^{3+} defects formed on the surface of TiO_2 with no change of morphology. Through one-step hydrothermal method at 200 °C, MoS_2 nanosheets *in situ* intercalated between $Ti_3C_2T_x$ layers using the $(NH_4)_6Mo_7O_{24}\cdot 4H_2O$ (AMT), $CS(NH_2)_2$ and oxalic acid as the precursor.[146] The $Ti_3C_2T_x$ layers played the role of a mechanical skeleton in supporting the MoS_2 nanosheets. To solve the poor oxygen resistance in air or oxygen-dissolved solution, a hierarchical MoS_2/Ti_3C_2@C nanohybrid was achieved by the *in situ* conversion of AMT and thiourea to MoS_2 nanoplates and the hydrothermal carbonization of glucose at 160 °C, followed by annealing at 500 °C in Ar flow.[147] The carbon nanoplating simultaneously proceeded around the scaffold of the MoS_2 nanostructure and Ti_3C_2 through the polymerization of glucose. Although significant efforts have contributed to the synthesis of MXene-based inorganic nanostructures, there is still enormous room for developing more efficient methods with improved control of the shape, size, crystallinity, exposure facet and functionality.

MXene-polymer composites Incorporating polymer into conductive MXene support provides a unique set of physic-chemical properties, including variable band gap, mechanical stiffness, controlled charge transport, film processability, and water solubility. MXene-polymer composites are basically prepared by solution mixing [97, 149-153] and *in situ* polymerization [154-157].

Solution mixing is a straightforward method for the synthesis of MXene-polymer composite. The solvent compatibility between MXene and polymer facilitates a good dispersity. Due to the terminal oxygen-containing functional groups, the negatively charged and delaminated $Ti_3C_2T_x$ colloidal solution can directly mix with either cationic polydiallyldimethylammonium chloride or electrically neutral polyvinyl alcohol (PVA) to produce $Ti_3C_2T_x$/polymer composites in aqueous solution.[152] Serving as the nanofiller, $Ti_3C_2T_x$ nanoplatelets were solution blended with poly(ethylene oxide) (PEO) dispersion to

prepare the PEO/$Ti_3C_2T_x$ nanocomposite.[151] The $Ti_3C_2T_x$ nanoplatelets with different concentrations affected the crystallization of poly(ethylene oxide) due to the heterogeneous nucleation and confinement effect. Dimethylsulfoxide intercalated MXene as the starting material could attract spontaneously the polymer solution between the layers. The water-soluble polyacrylamide/$Ti_3C_2T_x$ composite with good dispersion had been prepared via direct mixture.[150] Polar polymers with charged nitrogen-containing ends had the strongest interaction with the $Ti_3C_2T_x$ layers, expending the interlayer spacing better than nonpolar and polar but neutrally charged polymers.[149] After filtration or electrospinning,[153] MXene-polymer film and nanofibers could be formed.

In situ polymerization is the other method to modify MXene with polymers, such as polypyrrole (Ppy), polyethylenedioxythiophene (PEDOT), sodium alginate (SA) and poly(2-(dimethylamino)ethylmethacrylate) (PDMAEMA). In a typical process, after the etching of V_2AlC powders in aqueous HF at room temperature, the V_2C was mixed with the 2-(dimethylamino)ethylmethacrylate monomer.[157] The mixture was then exposed in ultraviolet light to initiate the polymerization reaction, and the PDMAEMA was grafted on the photo-active group functionalized surface of V_2C through self-initiated photografting and photopolymerization. With the aid of an external electrical field, the Ppy was intercalated into the Ti_3C_2 layers by electrochemical polymerization to form the Ppy/Ti_3C_2 composite films (Figure 4a).[156] At the immobilization stage, the Ti_3C_2 films were coated onto the surface of fluorine-doped tin oxide (FTO) using acetone and iodine as the stabilizer and charger, respectively. After the addition of the pyrrole monomer, the Ppy was electrochemically polymerized at a constant voltage of 0.8 V versus Ag/AgCl onto the FTO-coated glass with Ti_3C_2 particles to form individual Ppy/Ti_3C_2 clusters and finally the interconnected films. Without any external energy and oxidizing agent, the Ppy/$Ti_3C_2T_x$ composite was prepared by the simultaneous intercalation, alignment, and metal-free polymerization of pyrrole on $Ti_3C_2T_x$ (Figure 4a).[155] The $Ti_3C_2T_x$ layers not only had protonated pyrrole molecules due to the pronounced acidic character, leading to the formation of dimer and further polymerization, but also served as the template and substrate for the alignment of Ppy chains. Hydrogen bonding between the N–H group (or –OH, –COO, =O) of the pyrrole ring (or sodium alginate)

and the terminating oxygen or fluorine played key roles in the alignment process.[71, 155] A similar method had been extended to the *in situ* polymerization of 3,4-ethylenedioxythiophene (EDOT) onto $Ti_3C_2T_x$ via the electron transfer from each EDOT monomer to $Ti_3C_2T_x$ flakes upon adsorption.[154]

Other MXene-based composites The superior dispersion of MXene in different kinds of solvents makes for uniform multifunctional composites.[158] Other than inorganic nanostructure and polymer, various materials such as carbon nanotube (CNTs),[159-164] graphene,[23, 39, 165] carbon nitride,[166] carbon nanofiber,[167, 168] biomaterials,[98, 169] and metal-organic frameworks (MOFs)[170], have been hybridized with MXene for electrochemical applications. Most of these composites have been prepared by just blending the MXene or delaminated MXene dispersion with the other component solution. Typically, porous $Ti_3C_2T_x$/CNT heterostructured composites were realized by a self-assembly process.[163] As shown in Figure 4b, CNTs were firstly grafted by CTAB to obtain positively charged 1D CNTs. The CTAB/CNT solution was then added dropwise to the negatively charged $Ti_3C_2T_x$ suspension with the aid of sonication to form porous $Ti_3C_2T_x$/CNTs composites via electrostatic attraction. In particular, isolated $Ti_3C_2T_x$ nanosheets had recently been found to act as the supporting materials for *in situ* growth of MOFs (cobalt 1,4-benzenedicarboxylat, CoBDC).[170] The $Ti_3C_2T_x$ nanosheets were dispersed into a mixed N,N-dimethylformamide/acetonitrile solvent system with top, middle and bottom layers. After the addition of Co^{2+}, surface functional groups (-OH and -F) of $Ti_3C_2T_x$ in the top layer would immobilize the Co^{2+} ions via electrostatic interaction, which further coordinated with BDC molecules in the middle layer to form CoBDC/$Ti_3C_2T_x$ hybrids in an interdiffusion reaction assisted process. The CoBDC layers were seamlessly attached onto the electronegative surfaces of $Ti_3C_2T_x$ nanosheets, allowing fast charge and ion transfer, which was expected to favor the electrocatalytic processes.

4. The state-of-the-Art accomplishments of electrochemical devices

4.1. MXene-based electrode for supercapacitor

Supercapacitors are promising energy storage systems for futuristic energy consumption

devices with rapid power delivery or uptake, exceptional power densities (at least 10 kW Kg^{-1}) and better cyclability.[170] According to the charge-discharge mechanism, supercapacitors are classified into electrical double-layer capacitors and pseudocapacitors, in which most of the charge is transferred at or near the surface of the electrode material.[171-174] The former is based on the reversible accumulation (or electrosorption) of electrolyte ions at the electrode–electrolyte interface without redox reaction, while the latter depends on fast and reversible surface redox reaction for higher energy density.[55, 174] We have previously also reported on the porous carbon materials for the supercapacitor application.[172, 173] In search for alternatives in electrode materials, MXene, with layered 2D structure, good electrical conductivity, hydrophilic surface (-O, -OH and -F groups), flexibility and highly defined morphology, promises to provide rapid electron transfer channels and large electrochemically active surface for fast and reversible Faradic reaction.[22, 112, 56] The actual performances (specific capacitance and stability) of supercapacitors based on MXene materials are summarized in Table 1.

In 2013, the Gogotsi's group first demonstrated that the ions (i.e., T = Li^+, Na^+, Mg^{2+}, K^+, NH^{4+}, and Al^{3+}) that intercalated $Ti_3C_2T_x$ acting as flexible electrodes in aqueous electrolyte could induce a favorable volumetric capacitance of 350 F cm^{-3} at a 1 A g^{-1} scan rate with stable electrochemical cycling.[56, 108] In acid solution (H_2SO_4), the predominant electrochemical behavior of $Ti_3C_2T_x$ was pseudocapacitive. During the charge/discharge process, the cation could intercalate the interlayer gaps spontaneously and naturally, facilitating the electrochemical surface redox reaction in active transition metal oxide surface. A continuous change in the titanium oxidation state (TiO or TiO_2) produced rectangular-shaped cyclic voltammetry loops. Moreover, a conductive carbide layer could promote rapid charge transfer.[175] The adsorbed cations could be electrochemically inserted between partially swollen $Ti_3C_2T_x$ layers; charged small cations contracted the interlayer spaces of 2D electrodes, whereas larger cations with smaller charges expanded the interlayer spaces. As shown in Figure 5a, adsorption sites were involved in the hallow-adsorption sites near the edges of the water-rich multilayer particles and the deep-adsorption sites with higher activation energy for ion adsorption in the particle's interior.[176] After filling with ions and

water molecules, a perfect capacitive response over a surprisingly wide range of charging rates was generated.[176] Hydronium in H_2SO_4 electrolyte was involved in bonding with the O-termination in the $Ti_3C_2T_x$ negative electrode upon discharging, while debonding occurred upon charging (Figure 5b). The reversible bonding/debonding stemming from the surface functional group changed the valence state of Ti, accounting for the pseudocapacitance in the acidic electrolyte. Furthermore, counterion adsorption was accompanied by simultaneous co-ion desorption from the materials as ion exchange during discharging.[177, 178] However, in ionic liquid electrolyte, like the 1-Ethyl-3-methylimidazolium bis(trifluoromethylsulfonyl) imide (EMI-TFSI), the $Ti_3C_2T_x$ hydrogel film became accessible to EMI^+ and $TFSI^-$ ions because of disordered structure and stable spacing, and obtained a capacitance of 70 F g^{-1} together with a large voltage window of 3 V at a scan rate of 1 mV s^{-1}.[179] Under positive polarization, the electrostatic attraction between intercalated $TFSI^-$ anions and positively charged $Ti_3C_2T_x$ layers and/or steric effect deriving from deintercalation of EMI^+ cations resulted in a decrease of the interlayer spacing. In contrast, the steric effect of EMI^+ cation intercalation accounted for the observed increase of interlayer spacing under negative polarization.[180] The architectural design of $Ti_3C_2T_x$ electrode can improve ion accessibility to redox-active sites, inducing various pseudocapacitive performances. The 13-μm-thick macroporous $Ti_3C_2T_x$ film delivered a gravimetric capacitance of 210 F g^{-1} and 100 F g^{-1} at charge-discharge rates of 10 V s^{-1} and 40 V s^{-1}, respectively.[181] Also, the $Ti_3C_2T_x$ hydrogel electrode (1.2 mg cm^{-2} loading) enabled volumetric capacitance of up to 1,500 F cm^{-3}, which was comparable to the RuO_2-based electrode.

The capacitive performance of pure Ti_2CT_x electrode could be improved by various surface modification methods such as delamination, doping and calcination.[182-184] The substitution of terminal fluorine in Ti_2CT_x with functional oxygen-containing groups after chemical intercalation of potassium salts could give a capacitance of up to 520 F·cm^{-3} in H_2SO_4, which was four folds that of pure Ti_2CT_x.[183] The hydrazine-treated Ti_2CT_x electrodes as thick as 75 μm demonstrated a greatly improved capacitance of 250 F g^{-1} in acidic electrolytes with no capacitance degradation after 10000 cycles.[122] Serving as the intercalant molecules, hydrazine intercalated into $Ti_3C_2T_x$ reduced the amount of fluorine, -OH surface

groups and intercalated water, and thus facilitating the accessibility to active sites due to the pillaring effect between $Ti_3C_2T_x$ layers pre-opening the structure. It was also indicated that the heat treatment of Ti_2CT_x in Ar, N_2, and N_2/H_2 ambient could affect the capacitive performance, in which the specific capacitance value was 51 F g^{-1} at 1 A g^{-1} with superb rate performance (86%) and excellent cycling stability.[184] The thermal treatment in the N_2/H_2 atmosphere enhanced the carbon content and reduced the fluorine content, while retaining the original 2D layered morphology and providing the maximum access of aqueous electrolyte to the electrodes. It had recently showed that the nitrogen-doped delaminated Ti_3C_2 electrode (N-d-Ti_3C_2) exhibited a specific capacitance of 266.5 F g^{-1} in KOH aqueous solution, which was much better than that of N-graphene, N-porous carbon or Ti_2C.[185] It could be attributed to the synergistic effect of the layered structure, enlarged surface area, suitable distribution of pores and appropriate N atom doping level.

The 2D inorganic lattice of MXene provides an additional contribution of abundant active pseudocapacitive centers from various kinds of inorganic atoms or ions. In this regard, the improved electrochemical performance comes from not just the hierarchical structure (e.g., specific surface area), but also the chemical activity of the lattice framework. MXene has shown promising potential as flexible supercapacitor electrodes, but some challenges hinder the practical application as flexible supercapacitor, namely, (i) the contact between the $Ti_3C_2T_x$ blocks is poor due to the uneven sizes caused by the different numbers of titanium carbide layers; (ii) the volume changes (i.e., large expansion and contraction) of $Ti_3C_2T_x$ during the charge/discharge process in alkali hydroxide electrolyte; and (iii) the restacking of thin MXene flakes during paper production limits the accessibility to electrolyte ions and the electrode-electrolyte interaction, hindering the full utilization of active surface and countering the electron transport and ion diffusion. To mitigate the problems with practical implementation, MXene-based electrodes from hybrid structures such as $Ti_3C_2T_x$/polymer (e.g. PVA, Ppy), $Ti_3C_2T_x$/CNT, Ti_3C_2/TiO_2, $Ti_3C_2T_x/MoO_3$, Ti_3C_2/LDH, Ti_3C_2/ZnO, $Ti_3C_2T_x$/graphene and PANI@$TiO_2/Ti_3C_2T_x$, have been used extensively instead of a single ingredient.[139, 142, 143, 145, 152, 155, 156, 160, 165, 186, 187] For the Ppy/$Ti_3C_2T_x$ composite film, it exhibited a volumetric capacitance of 1000 F cm^{-3} with excellent cycling stability up to 25000

cycles in H_2SO_4 electrolyte.[155] The aligned conductive polymer chains between the conductive $Ti_3C_2T_x$ monolayers conferred many benefits in terms of electrical conductivity, reversible redox reactions, and short ion diffusion pathways. Combining the increased interlayer spacing and the surface redox processes of Ppy and $Ti_3C_2T_x$ led to an improved capacitance. Through the exfoliated Ti_3C_2 sheets bridging the NiAl-layered double hydroxide (LDH) nanoplates, a three dimensional porous conductive network was constructed to expose more active sites, facilitate the rapid electron transfer between electrolyte and active materials, and alleviate the volume change of LDH during the charge/discharge process.[145] Thus, the Ti_3C_2/LDH composite exhibited a specific capacitance of 1061 F g^{-1} at a current density of 1 A g^{-1} and capacitance retention of 70% after 4000 cycle tests. Excitingly, an asymmetric supercapacitor (ASC) device composed of NiO derived-TiO_2/C-$Ti_3C_2T_x$ nanocomposite as the positive electrode and $Ti_3C_2T_x$ as the negative electrode displayed an energy density of 1.04×10^{-2} W h cm^{-3} at a power density of 0.22 W cm^{-3}, and had cycling stability with 72.1% retention after 5000 cycles, better than the previously reported pure $Ti_3C_2T_x$ ASC.[144] The enhanced capacitive performance was attributed to the newly formed high-surface-area multilayer architecture, the active surface of NiO layer, and the favorable synergetic behavior of the $Ti_3C_2T_x$ negative electrode. Further, rGO nanosheets were inserted in between $Ti_3C_2T_x$ layers via electrostatic assembly for increasing the interlayer spacing and enabling more electroactive sites to be accessible to the diffusion of electrolyte ions.[187] As a standing electrode, this kind of symmetric supercapacitor displayed a volumetric energy density of 32.6 Wh L^{-1} with a maximum volumetric power density of 74.4 kW L^{-1}.

Flexible all-solid-state micro supercapacitors (ASSMSCs) without using a liquid electrolyte can be directly employed as embedded energy-storage devices for portable and wearable microelectronic systems. However, the improved performance of supercapacitors (e.g. electrical properties, mechanical integrity) by controlling the assembly of electrode along with the solid electrolyte and optimizing their ion transport remains a challenge. MXene materials are very promising for the high-performance ASSMSCs due to the favorable gravimetric capacitances with large packing density (4.0 g cm^{-3}) and the electrical conductivity of up to 6500 S cm^{-3}.[39, 188, 189] It has first reported the fabrication of $Ti_3C_2T_x$

ASSMSCs on the polyethylene terephthalate (PET) substrate with the size dimension of 1 cm × 3 cm using polyvinyl alcohol (PVA)/H_2SO_4 as the gel electrolyte.[188] This kind of ASSMSCs had fast charging and discharging capability and instantaneous power capability at a scan rate of 1000 V s^{-1}. The volumetric capacitance and energy density were 1.44 F cm^{-3} and 0.2 mWh cm^{-3}, respectively, at the current density of 0.288 A cm^{-3}. Furthermore, an all-MXene SSMCSs device was prepared by the spray-coating method, in which the stacked large-sized $Ti_3C_2T_x$ flakes with lateral dimensions of 3-6 μm served as current collectors at the bottom layer (Figure 6a).[189] Correspondingly, the small-sized $Ti_3C_2T_x$ flakes (~1 μm) with a large number of defects and edges were used as the electroactive layer responsible for energy storage at the top layer. Compared with Pt/s-$Ti_3C_2T_x$, the unique combination of L- and s-$Ti_3C_2T_x$ flakes reduced the large contact resistance from 20.4 Ω·cm^2 to 7.1 Ω·cm^2 between current collector and active materials, facilitating efficient charge transfer across the interface. Thus, for the flexible L-s-$Ti_3C_2T_x$ MSC, the areal capacitance value was 27.3 mF cm^{-2} at a scan rate of 20 mV s^{-1} and a capacitance retention of up to 100% was observed over 10000 cycles at a scan rate of 50 mV s^{-1} (Figure 6b). Moreover, the energy density value was 11–18 mW h cm^{-3} with corresponding power densities in the range of 0.7–15 W cm^{-3} (Figure 6c). Interestingly, it had reported that transparent (a transmittance of 93%) $Ti_3C_2T_x$ films with direct current conductivity of ~9880 S cm^{-1} could deliver a volumetric capacitance of 676 F cm^{-3}.[190] As a transparent supercapacitor device, it exhibited an area capacitance of 1.6 mF cm^{-2} and energy density of 0.05 μW h cm^{-2}, along with a long lifetime (i.e., no capacitance decay over 20000 cycles).

In general, the outstanding performance of all-MXene MSCs originates from the electrochemical characteristic of $Ti_3C_2T_x$ like the transformation of $Ti_3C_2T_x$ to TiO_2, good electrical conductivity, rapid intercalation between the sheets, fast pseudocapacitive contribution, and hydrophilic surface of MXene helping electrolyte infiltration. For resolving the disadvantage of relatively small size (~200 nm) for large-area flexible thin-film fabrication of MXene, it had recently proposed the flexible energy devices combining the $Ti_3C_2T_x$ nanosheets and electrochemically exfoliated graphene (EG).[39] In the hybrid electrodes, small-sized $Ti_3C_2T_x$ nanosheets between the graphene layers not only acted as

active materials and ideal “buffer” for enhanced electrolyte shuttling, but also functioned as conducting spacers to prevent the irreversible π–π stacking between graphene sheets. The MSC delivered a significant areal capacitance and volumetric capacitance as high as 3.26 mF cm^{-2} and 33 F cm^{-3}, respectively, at 5 mV s^{-1} (Figure 6d). In alternating flat and bent states, they had a long-term electrochemical stability with 82% of capacitance retention after 2500 cycles (Figure 6e). The good electrochemical energy output contributed to: (i) EG/MXene electrode affording plenty of large interlayer spacing and exhibiting a large accessible area for efficient ion adsorption and desorption; and (ii) graphene layers functioning as a mechanical skeleton to enhance the long-distance conductivity of electrodes. Moreover, the working potential window and energy storage capacity could be well-tailored by the series-parallel connection of as-fabricated ASSSs (Figure. 6f).

4.2. MXene-based electrode batteries

Lithium-ion batteries (LIBs) are one of the most commonly used power sources for wide-ranging portable electronic devices. For practical utility, new materials with high-capacity, lower polarization, longer duration and better stability are being rigorously pursued as reliable alternatives. In the recent four years, MXene, with superior theoretical Li storage capacity (447.8 mAh g^{-1} for Ti_3C_2 and 879 mAh g^{-1} for Mn_2C), favorable electronic conductivity, low operating voltage range, low diffusion barriers for Li mobility (0.018 eV for Sc_2C) and exceptional mechanical properties, has shown great promise for Li ion batteries (LIBs).[63, 194-195] The summary of capacity and cycling stability of MXene-based electrode materials for batteries is shown in Table 2. MXene-based electrode materials in LIBs can be divided into pure MXene (i.e. Ti_3C_2, $Ti_3C_2X_2$, Sc_2C, Ti_2C, Ti_3C_2, Ta_2C, Mn_2C, V_2C, Cr_2C, Nb_2C, Nb_2CX_2, V_2CO_2, Ti_3SiC_2, Mo_2CT_x and Ti_2CO_2) [63, 110, 121, 126, 194-217] and MXene-based hybrids (i.e. Ti_3C_2/carbon nanofiber, $Ti_3C_2T_x/Co_3O_4$, $Ti_3C_2T_x$/EDOT, $Ti_3C_2T_x/NiCo_2O_4$, Ti_2CT_x/Cu_2O, $Nb_2O_5@Nb_4C_3T_x$, $TiO_2@Ti_3C_2T_x$, Nb_2CT_x/carbon nanotube, Mo_2C/N-doped carbon, Nb_2O_5/C/Nb_2CT_x, $Ti_3C_2T_x$/Ag, $SnO_2@Ti_3C_2$ and CTAB−Sn(IV)@Ti_3C_2) [36-38, 40, 125, 136, 141, 154, 162, 167, 168].

Li ions adsorbed onto Ti_3C_2-based hosts form a strong Coulomb interaction. In the Ti_2C double layer, the binding energy was 0.2 eV, which was not sensitive to Li ions concentration

but decreased monotonically with biaxial strain.[199] Both Ti_2C strain and Li concentration could limit the diffusion of Li atoms. The diffusion barriers of bilayer structure are significantly higher than those of the corresponding monolayer, implying the more favorable use of dispersed monolayer MXene (M=Sc, Ti, V, or Cr) instead of multilayer in anodes.[205] Moreover, the Li-ions storage capacity are strongly dependent on the nature of surface functional groups, with -O groups exhibiting the most superior theoretical storage capacity.[198] Typically, ion adsorption reduced the electronic transport efficiency by more than 30% in Ti_3C_2 under the influence of localization/delocalization of electronic states, but, in the presence of oxygen groups in the termination of Ti_3C_2, the transport instead could be improved by ion adsorption by a factor of 4.[200] For the adsorption of first Li layer on V_2CO_2, surface O atoms would shift from H_2 to T sites (T was the top site directly above the V atoms on the top surface) as the Li ions concentration increased, leading to the H_1T-$V_2CO_2Li_2$ (H_1 was the hollow site directly above the C atoms) configuration due to more localized electrons and stronger bonding.[207] Furthermore, the stable H_2H_1T-$V_2CO_2Li_4$ (H_2 was the hollow site directly above the V atoms on bottom layer) configuration corresponded a Li storage capacity of 735 mAh g^{-1} and the O atoms were sandwiched between two Li layers, protecting additional Li atoms from forming Li dendrite. Substituting the O groups of MXene with other functional groups, the Li specific capacity could be predictably up to 259 mAh g^{-1} for S groups, 1264 mAh g^{-1} for P groups and 1767 mAh g^{-1} for Si groups. [215, 216]

It had been experimentally demonstrated that the exfoliated Ti_2C with lithiation and delithiation peaks at 1.6 V and 2 V vs. Li^+/Li, respectively, showed reversible capacity about 5 times higher than pristine Ti_2AlC.[197] As the anode for LIBs, Ti_3C_2 had a capacity of 123.6 mAh g^{-1} at 1C rate with a coulombic efficiency of 47%, higher than that of 2D Ti_2C because of the higher stability and larger space between Ti_3C_2 2D sheets to store Li ions.[110] Compared to pure Ti_2C, H_2O_2 oxidation of Ti_2C could increase the specific discharge capacity to 389 mA h g^{-1}, 337 mA h g^{-1}, 297 mA h g^{-1} and 150 mA h g^{-1} at current densities of 100 mA g^{-1}, 500 mA g^{-1}, 1000 mA g^{-1} and 5000 mA g^{-1}, respectively, after 50 charge/discharge cycles.[204] After 1000 cycles, a specific capacity of 280 mA h g^{-1} was retained. The improved performance had been deduced to be due to the larger surface area accessible to Li ions

resulting from the opening/swelling of Ti_2C layers with the formation of titania. For many commercial applications, the mass loading in Li anodes is beneficial to the area capacity. A binder-free MXene disc with a thickness of ~300 μm and a mass loading up to 50 mg cm^{-2} had been used as the anode.[202] It obtained an initial reversible areal capacity of 15 mAh cm^{-2} and 16 mAh cm^{-2} for Ti_3C_2 and Nb_2C, respectively. Only a 14% decrease occurred after 50 cycles. To minimize 2D nanosheets restacking, colloidal 2D titanium carbonitride had been produced and then used the freeze-drying Ti_3CNT_x with "fluffy" morphology (Figure 6g) as the electrode in LIBs.[212] The discharge capacity was 300 mAh g^{-1} at 0.5 A g^{-1} after 1000 cycles, which had been inferentially considered as the "electrochemical activation" process (Figure 6h). Specifically, the repeated cycling gradually exposed more fresh active sites to the electrolyte for accommodating more Li^+. The wettability of freeze-dried Ti_3CNT_x electrode favored the opening of more diffusion channels and thereby increased the capacity at various current densities. Interestingly, in contrast to the Li^+ diffusion coefficients (D_{Li+}, 6.27×10^{-11} cm^2 s^{-1}) of Ti_3CNT_x paper, the D_{Li+} of freeze-dried Ti_3CNT_x was 9.69×10^{-9} cm^2 s^{-1}, indicating that rational nanostructure design could lead to better capacity performance (Figure 6i).

The introduction of other components in MXene-based electrode could improve specific capacity and rate performance by the following aspects: (i) delaminating or pillaring MXene for storing more charge than their multilayer counterparts; (ii) improving ion accessibility and diffusion pathway to MXene layers; and (iii) hybridizing pure metal or metal compound with large capacity and excellent conductivity. The Gogotsi's group explored MXene/carbon nanotube composites for Li-ion storage devices.[121, 162, 206, 211] At 0.5 C, the Nb_2CT_x/CNT paper yielded a first-cycle capacity of ~780 mAh g^{-1} and a reversible capacity of ~420 mAh g^{-1}, with a coulombic efficiency close to 100%. Porous $Ti_3C_2T_x$/CNT films could obtain a capacity of 1250 mAh g^{-1} at 0.1 C and favorable capacity retention at relatively high current density. This can be presumably attributed to more Li ions that can be adsorbed and stored on the edges of pores in $Ti_3C_2T_x$ flakes. As a cathode material, the $Ti_3C_2T_x$/CNT paper could also give ~100 mAh g^{-1} at 0.1 C and ~50 mAh g^{-1} at 10 C. At 1 C, a capacity of 80 mAh g^{-1} was maintained after 500 cycles with the coulombic efficiency of 100%. In the half-cell studies, as shown in Figure 6j, the Nb_2CT_x/CNT-based cell could operate within 3 V voltage windows

and deliver capacities of 24~36 mAh g^{-1} (per total weight of two electrodes in each cell) with the volumetric energy density of 50-70 Wh L^{-1}. Other groups have followed similar strategies via the integrated utilization of MXene with pure metal or metal compounds. It was demonstrated that Ag/$Ti_3C_2(OH)_{0.8}F_{1.2}$ had reversible capacities of 310 mAh·g^{-1} at 1 C, 260 mAh·g^{-1} at 10 C, and 150 mAh·g^{-1} at 50 C, and furthermore the steady-state capacity of 150.0 mAh·g^{-1} at 50 C after 5000 cycles could be sustained due to the reduced interface resistance and the appearance of Ti(II) to Ti(III) during the cycle process.[36] After incorporating the Cu_2O particles with Ti_2CT_x for LIBs anode, Zhang et al.[37] obtained a discharge capacity of 143 mAh g^{-1} at a discharge current density of 1000 mA g^{-1}, and the capacity retention was near 100% after 200 cycles. It has been presumed that the Cu_2O nanoparticles grown between the stacked Ti_2CT_x sheets not only formed open electrically conductive frameworks for improving charge transfer and reducing the capacity loss, but also contributed more sites for improving specific capacity. Similar work had been shown by Wang et al. [136] for the SnO_2/Ti_3C_2 nanocomposite with a capacity of 360 mAh g^{-1} after 200 cycles at a discharge current density of 100 mA g^{-1}. The Sn^{4+} ionic conductivity in SnO_2 nanoparticles was important for improving the conductivity and Li^+ insertion/extraction into the anode. Tao's group successfully demonstrated that the Sn(IV) aggregates in the alkalization intercalated Ti_3C_2 matrix did not only accommodate strain induced by the volume change, but also confined the occurrence of Sn(IV) detached from the matrix during the electrochemical reaction processes.[126] Thus, this kind of electrode gave rise to a volumetric capacity of 1375 mAh cm^{-3} (635 mAh g^{-1}) at 216.5 mA cm^{-3} (100 mA g^{-1}) with a capacity retention of 42.5% after 50 cycles and a stable discharge capacity of 504.5 mAh cm^{-3} (233 mAh g^{-1}) at a current density of 6495 mA cm^{-3} (3 A g^{-1}). Very recently, they had testified the role of "pillar effect" in MXene-based electrode using the CTAB prepillaring and Sn^{4+} pillaring Ti_3C_2 (Figure 7a,b).[125] The "pillar effect" caused more Li^+ being intercalated in the interlayer of Ti_3C_2 shortened the ion-diffusion path, and reduced the resistance of ionic diffusion and charge transfer with the aid of the Sn(IV) nanocomplex. Thus, the specific capacity was 506 mAh g^{-1} with the capacity retention of 96.9% at the current density of 1 A g^{-1} after 250 cycles. As the anode of lithium-ion capacitors (Figure 7c), the outstanding

energy density was 239.50 Wh kg^{-1} at the power density of 10.8 kW kg^{-1}. The capacity retention was 71.1% even after 4000 cycles at 2 A g^{-1} and the columbic efficiency was ~100% during the cycling test (Figure 7d). Therefore, it can be expected that, in the use of pillared MXene as model materials, studying the adsorption/intercalation of multivalent metal ions is one of the principal challenges in electrochemical energy storage. Although significant advances have been made, the specific capacity of MXene-based materials remains relatively low when used as the electrode materials of Li-ion batteries (LIBs). This is in part because the vast majority of MXene produced are usually terminated with surface groups such as hydroxyls and fluorines, whose steric hindrance effect increases the diffusion barrier of Li ions and thereby affects the performance of the LIB anodes. Furthermore, after incorporating Li ions into the lattice of MXene, the possible disintegration of the nanostructures resulting in smaller and thinner nanoparticles may further obstruct lithium-ion storage. The development of approaches for controlling the surface chemistry of MXene and introducing other active components is important for improving electrode materials for the next generation of batteries.

MXene-based electrodes have also captured many researchers' attention in Li–S batteries with the theoretical energy density of 1675 mA h g^{-1}. As the conductive sulfur hosts, the strong interaction of polysulfide species with surface Ti atoms of MXene can solve the following problems:[218, 219] (i) the volume expansion of sulfur during the charge/discharge process; (ii) the low electrical conductivity of the electrode; and (iii) the shuttle effects of lithium polysulfide. The $Ti_3C_2T_x$ nanosheets-coated commercial "Celgard" membrane was used as the separators to enhance the cyclability and reversibility in sulfur/carbon black composite cathodes of the Li–S battery (Figure 7e).[220] It has been inferred that the electrically conductive $Ti_3C_2T_x$ acted as a second current collector to reduce the internal resistance of each cell, facilitating faster redox kinetics. More interestingly, the formed coating layer with a highly polar active surface became a reservoir for immobilizing soluble polysulfide from the cathode region of the cell via both physisorption and chemisorption, suppressing the shuttling effect of polysulfide. Serving as the anchoring materials in Li-S batteries cathodes, the 70 wt% S/Ti_2C composites covalent by S-Ti-C bond obtained a specific

capacity of ~1200 mA h g^{-1} at a five-hour charge/discharge (C/5) current rate (Figure 7f) and a capacity retention of 80% over 400 cycles at a two-hour charge/discharge (C/2) current rate.[221] The interfacial interaction between metallic Ti_2C phases and polysulfide presented a dual mode behavior, which was termed as "Lewis acid–base interaction and thiosulfate/ polythionate conversion" (Figure 7g).[164] Polysulfides were firstly reacted with the terminal hydroxyl groups on the Ti_2C surface via redox reaction to generate thiosulfate, and then the Ti-S bonds by Lewis acid-base interactions formed via the exposed and metastable Ti atoms readily accepted electrons from the additional polysulfide in the electrolyte. After interweaving CNTs into this kind of system, a capacity of ~450 mA h g^{-1} at a C/2 rate were retained after 1200 cycles, corresponding to a decay rate of merely 0.043% per cycle.[164] Moreover, a stable and available capacity was 910 mA h g^{-1} when the practical sulfur loading electrodes was up to 5.5 mg cm^{-2} (Figure 7h). The excellent performance had confirmed the synergistic effect between the improved conductivity and surface area, and the effective polysulfide chemical absorptivity on the sulfur host material. From the theoretical viewpoint, Sim et al.[222] provided an understanding about the suppression of the shuttle effect, which had been dominantly affected by the interaction between the functionalized surface of Ti_2CO_2 and the lithium polysulfide (LiPSs). As an example, the O-functionalized surface converted soluble lithium polysulfide (e.g., Li_2S_8, Li_2S_7, Li_2S_6) to insoluble elemental sulfur.[222, 223] Transition-phase Ti_2CO_2 supported the redox reaction to form LiPSs intermediates via supplying its own free electrons. This research provided a preliminary relationship of the surface functionality and the lithium polysulfide transformation for improving the performance of Li-S batteries.

Apart from the LIBs and Li–S batteries, some efforts have been devoted to replacing Li by other abundant alkali-metal elements (e.g., Na-, K-, Mg-, Ca- and Al-ion), based on the accommodation of various ions sizes between the 2D layers of MXene.[121, 146, 163, 214, 224-231] The light transition metals-based MXene with non-functionalized or O-terminated surfaces exhibited an anode voltage in range of 0.2-1.0 V and good gravimetric capacity, as shown in Figure 8a.[214, 228] The Na- and K- ions were usually intercalated into the terminated MXene, and the Mg and Al ions were stored via stable multilayer adsorption with the aid of the

combination of conversion reaction, insertion/extraction, and plating/stripping metal ion storage mechanism.[228] Taking the Na ions battery as an example, a Na-ion full cell prototype consisting of an alluaudite $Na_2Fe_2(SO_4)_3$ positive electrode and a Ti_2C negative electrode operated at a voltage of 2.4 V and delivered 90 and 40 mAh g^{-1} at 1.0 and 5.0A g^{-1}, respectively (Figure 8b). The specific energy was 260 Wh kg^{-1} at a specific power of 1.4 kW kg^{-1}.[226] As the positive electrode for sodium-ion capacitor, V_2CT_x stored energy through intercalation of Na ions between layers and showed an achieved capacity of 50 mAh g^{-1} with a maximum cell voltage of 3.5 V.[224] The Na ions were electrochemically intercalated/deintercalated into/out of the $Ti_3C_2T_x$ lattice reversibly *via* two-phase transition and solid-solution reaction in sequence.[230] During sodiation, compared to bare Ti_3C_2, the F- and O- functionalized Ti_3C_2 had small changes of lattice constants and low barriers for sodium diffusion.[227] Na ions preferred to occupy the top sites of the C atoms in the monolayer $Ti_3C_2T_x$ due to the adsorption energy of 0.946, 0.598 and 2.138 eV for Ti_3C_2, $Ti_3C_2F_2$ and $Ti_3C_2O_2$, respectively.[227, 230] The occupied Na^+ enlarged the interlayer distance of $Ti_3C_2T_x$ from 9.7 to 12.5Å during the first sodiation process, and then it carried out the reversible intercalation/deintercalation of desolvated Na^+ between the $Ti_3C_2T_x$ layers (Figure 8c).[225] Interestingly, this electrochemical reaction process had not caused the change of interlayer distance due to the pillaring effect of trapped Na^+ and the swelling effect of penetrated solvent molecules between the $Ti_3C_2T_x$ sheets.[225] Such features extended the application of MXene-based electrodes as promising potential candidates for Na^+ energy storage devices.

Recently, using other components as pillars, like MoS_2 and carbon nanotube (CNT), in MXene-based electrodes has given rise improvement in the capacity of sodium-based energy storage devices. Using porous Ti_3C_2/CNT composites as freestanding paper electrodes, the volumetric capacity was 421 mA h cm^{-3} at 20 mA g^{-1} with good rate performance and cycling stability.[163] The as-assembled cell could power a 2.5 V light-emitting diode for ~25 min, with an energy consumption of 0.041 mW h^{-1} (Figure 8d). Wu et al. intercalated the MoS_2 nanosheets into $Ti_3C_2T_x$ layer, and boosted the specific capacity to 250.9 mA h g^{-1} over 100 cycles and the rate performance with a capacity of 162.7 mA h g^{-1} at 1 A g^{-1}.[146] It had been

hypothesized that the expanded interlayer benefited more active sites for sodium reaction and a lower barrier for Na^+ insertion and adsorption. Also, the open structure was favorable for shortening the Na^+ diffusion pathway and buffering the volume changes of MoS_2 during the sodiation/desodiation processes. Moreover, the highly conductive $Ti_3C_2T_x$ as a substrate provided an effective electron transfer path.

5. Emergence and prosperity of MXene-based photo-electrocatalyst

5.1 MXene-based photocatalyst

Photocatalysis, which is one of the advanced catalysis technologies and is an important route for solar-to-chemical energy conversion, has been widely studied for chemicals synthesis, energy production and environmental purification.[171, 232-236] An abundance of photocatalyst has been explored to extend the efficiency of light absorption and conversion and the chemical energy utilization. Our previous studies have focused on the material synthesis and photocatalytic application of two dimensional materials like graphene, carbon nitride and metal sulfide.[237-241] There remains room for exploring new photocatalyst. In recent years, it has been demonstrated that quite a few $M_{n+1}X_nT_x$ are narrow band gap semiconductors, which can be tuned by altering their surface chemistries (e.g. the terminated -F, -OH, or -O groups) or the arrangements of surface groups relative to the M atoms for satisfying the requirements for photocatalysis application.[63, 67, 148] Moreover, for the $M_{n+1}X_nT_x$ like 2D Zr_2CO_2 and Hf_2CO_2, the significant and directionally anisotropic carrier mobility (Figure 8e) benefited the separation and migration of photogenerated electron–hole pairs.[59] It had first been observed that $Ti_3C_2T_x$ degrades methylene blue and acid blue 80 with degradation efficiencies of 81% and 62%, respectively, during ultraviolet (UV) irradiation over 5 h.[242] The formation of titanium hydroxide and/or TiO_2-both on the $Ti_3C_2T_x$ surfaces contributed to the photocatalytic effect. However, the single-component MXene photocatalyst displayed low photocatalytic activity due to fast recombination of photogenerated electrons-holes pairs, narrow light-absorption range, and limited stability in oxygen-obtained water. To overcome these disadvantages, using 5wt% $Ti_3C_2T_x$ as a co-catalyst with rutile TiO_2, a 400% enhancement had been obtained in photocatalytic

hydrogen evolution reaction from water splitting compared with that of pure rutile TiO_2 under visible light condition.[243] The metallic $Ti_3C_2T_x$ not only provided a 2D platform for the uniform growth of TiO_2 nanoparticles via intimate interactions, but also served the role of electron sink to promote the separation of photogenerated charge carriers via the Schottky barrier.

The photoexcitation of photocatalyst is structurally sensitive to the surface energy and atomic configuration of crystalline facets, and thus leads to the different photogeneration rate of electron−hole pairs and the direction of charge transfer between two components. A hybrid of Ti_3C_2 nanosheets and TiO_2 selectively exposing {001} facets conferred efficient photogeneration of the electron−hole pairs.[140] The carrier separation was substantially promoted by the hole-trapping effect through the interfacial Schottky junction (Figure 8f), with the 2D Ti_3C_2 acting as a hole reservoir. The interface formation originated from the overlapping of the Ti d-orbital and the O p-orbital, as shown in Figure 8g,h. In methyl orange degradation process, the {001}TiO_2/Ti_3C_2 exhibited a 2.3-fold higher degradation rate constant than p-TiO_2/Ti_3C_2 under UV exposure. The work function (ca. 1.8 eV) of OH-Ti_3C_2 was lower than that of the {001} surface in TiO_2 (ca. 4.9 eV), because the photogenerated holes, instead of electrons, could be injected from TiO_2 to OH-Ti_3C_2. The Schottky barrier at TiO_2/Ti_3C_2 interfaces could effectively prevent the holes from flowing back to TiO_2. In the later study, it had further reported that increasing the NH_4F concentration during the synthesis process could induce the transformation of TiO_2 octahedrons from (110) facets to (111) facets, leading to improved photocatalytic activity (Figure 9a,b). After the treatment of hydrazine hydrate, there was no change in the crystallographic structure and morphology of (111) r-TiO_2/Ti_3C_2, but the lattice vacancy induced by the Ti^{3+} dopant embedded within the bulk of TiO_2 extended the photocatalytic activity to the visible light range.[92] Very recently, the Qiao group explored the potential of Ti_3C_2 nanoparticles as highly efficient co-catalysts in cadmium sulfide for photocatalytic H_2 evolution reaction (HER).[41] This kind of photocatalyst can induce an outstanding visible-light photocatalytic hydrogen production activity of 14342 mmol h^{-1} g^{-1} with an apparent quantum efficiency of 40.1% at 420 nm. More importantly, they presented an in-depth understanding of the superior HER activity based on

first-principles energy and band structure calculation. The Gibbs free energy of intermediate state (adsorbed H*, ΔG_H) for O-terminated Ti_3C_2 was a near-zero value of 0.00283 eV, which was much lower than that of Pt or highly active earth-abundant HER catalysts (Figure 9c). Combining favorable Fermi level position and the electrical conductivity of Ti_3C_2 NPs favored the highly efficient charge separation and migration from CdS to Ti_3C_2 NPs, as shown in Figure 9d, resulting in rapid H_2 evolution on numerous O terminations presented on Ti_3C_2.

Overall, pure MXene has poor photon absorption and suffers from high rate of charge carrier recombination. It has provided the needed impetus for designing MXene-based nanoarchitectures to increase the light harvesting ability, attain satisfied quantum efficiency and enhance the carrier separation with efficient solar-to-chemical applications. Moreover, these works presented the synthetic strategy give an inspiration to design well-contacted heterojunction interface between MXene and the other nanoparticles for superior photoredox efficiency in photocatalysis and energy conversion.

5.2 MXene-based electrocatalyst

Electrochemical systems, such as fuel cell, CO_2 reduction and water splitting devices, represent efficient and environmentally friendly technologies for energy conversion and storage.[244-246] Electrocatalyst play key roles in the electrochemical process but often limit the performance of entire systems due to insufficient activity and lifetime. In our previous research, it has been demonstrated that various electrocatalyst including graphene-based derivatives, nitrogen-doped carbon, metal carbide/phosphide showed outstanding electrocatalytic activity in the field of hydrogen evolution reaction, oxygen evolution reaction and carbon dioxide reduction.[247-249] However, it has been a long-standing challenge to develop efficient and durable electrocatalyst. MXene have been predicted to be potential heterogeneous catalysts because of the combination of superior electrical conductivity, surface hydrophilicity and good stability.[128] Moreover, as a class of materials with ultralow work function and electronegative surfaces, MXene are potential supporting materials, which may alter the electrophilicity of active centers of catalysts and thereby tune the electrochemical properties in multi-component electrocatalyst systems.

Water electrolysis to produce clean fuel is a promising solution for both the energy and environment crises. For the first time, Seh et al.[250] theoretically and experimentally demonstrated that with a small ΔG_H of 0.048 eV, Mo_2CT_x performed as an active and stable catalyst for HER in acid. Compared with Ti_2CT_x, the Mo_2CT_x exhibited far higher HER activity with an initial overpotential of 283 mV to reach 10 mA cm^{-2}_{geo} and an average turnover frequency of ~0.01 H_2 s^{-1} at 200 mV overpotential. They speculated that the basal planes of Mo_2CT_x were catalytically active towards HER, unlike in the case of the widely studied MoS_2, in which only the edge sites of the 2H phase were active. With a high portion of exposed metal atoms on the surface, the Mo_2CT_x suffered from poor oxygen resistance, causing a significant loss of electronic properties and surface reactivity. To address this, the Ti_3C_2 was stabilized by carbon-nanoplating for developing hierarchical MoS_2/Ti_3C_2@C electrocatalyst, with an onset potential of -20 mV, a overpotential of 135 mV, a Tafel slope of 45 mV dec^{-1} and an exchange current density of 29 μA cm^{-2}, which is better than that of Pt/C, MoS_2/rGO@C and MoS_2/oxidized MXene catalysts (Figure 10a).[147] Moreover, the electrocatalyst showed good stability and duration in an acidic solution (Figure 10b). It had been proposed that the excellent performance was attributed to the synergy of carbon nanoplating, Ti_3C_2 and MoS_2 nanostructure, which led to greatly enhanced electrical properties, structural stability and reaction kinetics for electrochemical reactions (Figure 10c). In particular, the presence of carbon over-layer around the scaffold of MoS_2/Ti_3C_2 may not only prevent the corrosion, detachment and electrical isolation of active materials, but also help to reduce the H_2 adoption to a moderate value. The Ti_3C_2 promoted the electronic coupling with MoS_2 nanostructures and acted as the 2D highway for fast and smooth charge transfer. Few-layered MoS_2 nanoplates imparted the more active edge sites and the extremely shortened pathway for mass diffusion and charge transfer. The CVD-synthesized Mo_2C/graphene with high crystallinity and low defect had been used as an electrode, which showed a low overpotential value of 236 mV, better than the reversible hydrogen electrode with an onset potential of 87 mV for a current density of 10 mA cm^{-2}.[127] Also, the Tafel slope was 73 mV dec^{-1} with favorable durability. However, one of drawbacks of MXene as electrocatalyst is the strong hydrogen adsorption capacity, which greatly affects the HER

performance. Taking V_2CO_2 as an example, it has theoretically predicted that the introduction of transition metals like Co, Ni and Fe could greatly weaken the bonding interaction between hydrogen and oxygen.[251] By choosing the suitable type and coverage of the promoters as well as the active sites, the hydrogen adsorption free energy could reach an optimal value of ~0 eV. Therefore, the 2D MXene with metal doping opens a new window for developing cost-effective alternatives to Pt in HER.

Developing efficient and cost-effective electrocatalyst for oxygen-evolution reaction (OER) is of great significance, since the OER is coupled with key clean energy systems like electrolytic/solar water splitting and rechargeable metal–air batteries. Qiao and co-workers reported a free-standing flexible hybrid film (TCCN) of overlapping g-C_3N_4 and Ti_3C_2 nanosheets for catalyzing OER in alkaline solution.[166] As the working electrode in 0.1 M KOH solution, this film delivered a current density (E_j = 10) of 1.65 V, a Tafel slope of 74.6 mV decade^{-1} and a Faradaic efficiency of 95.5%. The stable and rosy performance of OER, dominated by the four-electron pathway with negligible peroxide intermediate formation, had been proven to originate from the Ti–N_x motifs between g-C_3N_4 and Ti_3C_2 nanosheets acting as electroactive sites, and the hierarchically porous structure with highly hydrophilic surface. Interestingly, MXene can be as supporter and reductant simultaneously for the *in situ* formation of metal nanoparticles, leading to the enhancement of conductivity. Analogously, the MXene-$Ag_{0.9}Ti_{0.1}$ bimetallic nanowire composite has been prepared, in which the low valence Ti species resulted in the formation of metallic Ag.[131] As an electrocatalyst in the oxygen reduction reaction (ORR), it exhibited an onset potential of 0.921 V and a half-wave potential of 0.782 V vs RHE (reversible hydrogen electrode, RHE). After 1000 cycles, the least reduced amount (0.016 V vs RHE) revealed the structural stability and reversibility due to the unique morphology and electron structure. With the layered support, nanowire and Ag-Ti interfaces, it has also displayed exceptional electrochemical activity in oxygen reduction reaction (ORR) by enhancing conductivity and active sites (defects or vacancies), making it comparable to the commercial Ag/C catalyst and pure Ag nanowire. Very recently, Zhao et al.[60] explored a hybrid of 2D cobalt 1,4-benzenedicarboxylate (CoBDC) with $Ti_3C_2T_x$ via inter-diffusion reaction for ORR (Figure 10d). It achieved the lowest onset

potential of 1.51 V vs RHE, a current density of 10 mA cm^{-2} at a potential of 1.64 V vs. RHE, and a Tafel slope of 48.2 mV dec^{-1} in 0.1 M KOH, which was asserted to outperform the standard IrO_2-based catalyst and even the transition metal-based catalysts (Figure 10e,f). The superior performance resulted from the synergistic coupling effects between the two components via the well-defined interface. On the one hand, the 2D CoBDC layer provided the highly porous structure and large surface area with Co-based active species. On the other hand, the electrically conductive and hydrophilic $Ti_3C_2T_x$ nanosheets enabled the rapid charge and ion transfer across the well-defined $Ti_3C_2T_x$/CoBDC interface and facilitated the access of aqueous electrolyte to the catalytically active CoBDC surfaces. Meanwhile, the metal-like $Ti_3C_2T_x$ nanosheets improved the charge transfer kinetics by converting the oxygen evolution from a charge transfer-limited process to a reaction-limited one. Thus, MXene-based materials pave a new pathway for designing novel electrocatalyst in electrochemical system.

6. Summary and Perspective

Recent advances on pure MXene and their hybrids have been summarized as an emerging platform for electrochemical devices and photo-electrocatalyst. The attractive properties of MXene such as metallic conductivity, tunable band gap structure, unique carrier anisotropic mobility, transparency and absorption, good Young's modulus, and superior optical and thermal performance enable it to be a promising 2D material for constructing multifunctional nanostructures with flexibility and versatility. The synthesis of pure MXene from monolayer to multilayer has been successfully carried out by the direct etching methods and their auxiliary ways like, sonication, delamination or molecular intercalation. Although many challenges abound, the direct synthesis of pure high-quality MXene by bottom-up methods like CVD have bright prospects due to the enhanced control of structure and defects. For MXene derivatives, several kinds of hybrid materials like polymer, metal/metal compound and carbon materials have also been constructed, for instance, through blending mixture, chemical reduction, calcination and (hydro-) solvothermal process, combination with nanoparticles, 1D nanowire, and assembly with other 2D materials. As for practical applications, taking advantage of their unique traits and properties, MXene has exhibited

exciting performance in supercapacitors, batteries, photocatalysis and electrocatalysis (e.g., HER and OER). In particular, MXene-based hybrids have been proven to further improve the performance by synergistic effects derived from the hybrid interfaces.

Equipped with a wide range of extraordinary properties, MXene hence promises a broader spectrum of novel applications beyond electrochemical devices and photo-electrocatalyst, such as sensor, membrane separation, photothermal conversion and hydrogen storage. Liu et al.[169] showed that hemoglobin immobilized Ti_3C_2 had a nitrite detection linear range of 0.5–11800 μM, with a lower detection limit of 0.12 μM due to the direct electron transfer of Hb, the large surface area and the high conductivity of Ti_3C_2. The $Ti_3C_2T_x$ could be used as a H_2O_2 sensor by electrochemical reactions in a cathodic potential window and the detection limitation was as low as 0.7 nM with a response time of ~10 s.[46] The field of membrane separation benefited from the 2D structure, micrometer-thick MXene membranes constituted by 2D $Ti_3C_2T_x$ nanometer-thin sheets, which gave a water flux of 37.4 L $Bar^{-1}·h^{-1}·m^{-2}$ and also had charge- and size-selective ion-sieving ability due to the flexibility, high mechanical strength, hydrophilic surfaces, and electrical conductivity.[252] After being supported on anodic aluminum oxide substrates with the aid of $Fe(OH)_3$ colloidal intercalated particles, the 400 nm-thick $Ti_3C_2T_x$ membrane obtained a water permeance of 1084 Lm^{-2} h^{-1} bar^{-1} and superior molecules rejection efficiency of 90%, 100%, 100% and 93%, for evans blue, bovine serum albumin, gold nanoparticles and cytochrome, respectively.[45] The fresh $Ti_3C_2T_x$ membranes had the antibacterial rate of more than 73% against B. subtilis and 67% against E. coli, while over 99% growth inhibition of both bacteria could be obtained after aging under the same conditions, which was due to the occurrence of oxidative stress (i.e., reactive oxygen species) via the synergistic effect between the $Ti_3C_2T_x$ nanosheets and TiO_2/C formed on the surface.[253, 254] Li et al. found that the internal light-to-heat conversion efficiency of Ti_3C_2 was 100%, and, as a self-floating MXene thin membrane, it could produce a light-to-water evaporation efficiency of 84% under solar irradiation.[48] Furthermore, MXene such as Ti_2C, Sc_2C, V_2C and Cr_2C are also promising as hydrogen storage materials or catalysts for hydrogen storage in hydrides.[255-258] For example, Ti_2C with the binding energy of 0.272 eV exhibited 3.4 wt% hydrogen storage capacity.[255] The hydrogen molecules bound by

Kubas-type interaction could be adsorbed and released reversibly under ambient conditions. Wu et al. experimentally demonstrated that the dehydrogenation/hydrogenation performance of $NaAlH_4$ in the presence of 7 wt% Ti_3C_2 could be improved via the reduction reaction between Ti_3C_2 and $NaAlH_4$, and the formation of metallic Ti to Ti^{3+} species.[256] Approximately 4.7 wt% hydrogen could be released within 100 min at 140 °C, and the dehydrogenated sample could absorb 4.6 wt% hydrogen within 60 min at 120 °C. Similarly, serving as a catalyst, Ti_3C_2 with superior catalytic effect also enhanced the hydrogen storage reaction of MgH_2 because of the layered structure and the *in situ* formed metallic Ti.[257] Thus, the MgH_2/Ti_3C_2 hybrids could release 6.2 wt% hydrogen gas within 1 min at 300 °C and absorb 6.1 wt% hydrogen gas within 30 s at 150 °C. These discoveries inspire the development of MXene towards wider applications, like environmental remediation, water resource regeneration, chemical detection and photothermal tumor therapy.

Despite the significant progress that has been made, the research with respect to MXene-based electrode and catalyst is lagging far behind in comparison with other 2D counterparts such as graphene and TMDs. Initial studies have identified many challenges as well as opportunities. One of the greatest advantages of MXene is the plentiful selection of type and composition, as well as the proportion and arrangement of different atoms, which provides great opportunities to design these materials at the atomic level. Although many kinds of MXene have been theoretically calculated and designed, the experimental synthesis and testing of practical application are urgently needed. While the current research has mainly focused on MXene preparation from raw MAX materials, the modification of the raw MAX phase like the A substitution could herald a new generation of MXene. It has been preliminarily shown that the Si atoms-layer of Ti_3SiC_2 could be substituted by noble metals to produce Ti_3AuC_2, $Ti_3Au_2C_2$ and Ti_3IrC_2 through an ordered exchange on specific crystal planes.[259] This can be considered as a new route to prepare noble metal-based MXene. The pillared structure of MXene provides a superior platform to study the adsorption /intercalation of ions inside the host structure, which is also one of the main challenges in electrochemical energy storage. During the electrochemical process, the interaction of electrolyte ions and host surface strongly depends on the interlayer spacing of MXene, which can be fine-tuned by

selecting the types of surfactant molecules and ions. Moreover, the properties of MXene are highly sensitive to layer number, flake size, terminated group species, chemical functionality, different phases (H-/T-phase or transition phase), vacancy and defect. It is necessary to precisely control these parameters in the local reaction environment, including temperature, solvent, functional molecular and possible soft-templates.

Based on the advantages of MXene in both structure and property, hybrid systems and the corresponding synthesis methods need to be further developed. For instance, the layer space in multilayer MXene could be fulfilled by functional molecules and low dimensional nanomaterials, which further impact their catalysis, photochemical and electrochemical activities via the synergistic effect. For the ultrathin or monolayer MXene, the modification process can gain from research on graphene-based hybrid systems. One example is the plane-to-plane heterostructure or van der Waals heterostructure, such as graphene–MXene, layered metal oxide/sulfide–MXene and LDH–MXene, and many similar systems, which have been demonstrated to possess superior performance in electrochemical energy conversion and electro- /photocatalysis. Developing 2D layered materials with active basal planes to construct the mixed low dimensional heterostructure (0D-2D and 1D-2D) and even the 3D architecture is an interesting research direction for high-performance electrode and catalyst. Moreover, ample groups on the surface of 2D materials could not only be modified by functional molecules or substituted by other groups (Br, Cl, I or hydrophobic groups) to tailor the intrinsic properties, but also become the attached sites for the direct growth of other nanostructured materials. Future research on this area is conducive to gather an in-depth understanding on the unique surface environment of MXene. Another interesting hybrid form of MXene is the 2D in-plane heterostructure, which needs to be developed in the field of 2D materials. It had recently been demonstrated that MXene could be a confined soft-template to prepare the layer-by-layer porous carbons or titanate nanoribbons.[260, 261] The in-plane heterostructure of MXene and modified MXene can be synthesized through the partial conversion of MXene nanosheets to other species by reduction, oxidation or substitution reactions without any structural change. All in all, this hybridization strategy is facile and flexible, and can be extended for preparing a large number of MXene-derived materials for

various applications such as supercapacitors, batteries, and advanced catalysis.

From the perspective of practical applications, although the MXene-based electrode has shown great potential in supercapacitors, Li ions, Li-S, or Li-O_2 batteries, many questions remain regarding the electrochemical conversion mechanisms based on MXene. For instance, aqueous rechargeable lithium batteries show promising potential in high-energy batteries since the aqueous electrolyte has favorable ionic conductivity and solubility, rich natural resources, and environmental friendliness. The interlayer water molecules affect the elastic properties of MXene and the ionic transport in the 2D layers in liquid electrolyte. Developing characterization methods like scanning probe microscopy techniques with improved spatial and time resolution are very promising for imaging the viscous losses, water molecules arranged structure and elastic dynamic characterizations, which would help to further improve the electrode performance. Emerging Li-X (X = Se, Te, I_2, Br_2) batteries have similar electrochemistry to Li-S batteries and excellent physical properties (e.g., electronic conductivity and tap density). Thus, it is expected that the progress of MXene in these emerging Li-X (X = Se, Te, I_2, Br_2) batteries will open up new opportunities in battery systems.

MXene provides an expansive platform for the field of advanced catalysis such as photocatalysis, electrocatalysis and photoelectrocatalysis. The current research mainly focuses on HER, ORR, OER and pollutant degradation, but there is still no in-depth understanding on CO_2 catalytic transformation and N_2 fixation. Simulations have indicated that the monolayer Ti_2CO_2 could photocatalyze CO_2 reduction at the oxygen vacancy sites, and a reaction pathway like $CO_2 \rightarrow HCOO \rightarrow HCOOH$ with an energy barrier of 0.53 eV was proposed.[262] The CO and H_2 can introduce sufficient oxygen vacancies on O-terminated MXene. More importantly, the catalytic mechanisms in the presence of MXene are quite complicated and warrant further in-depth studies. It is necessary to elucidate the crucial roles of catalytically active sites and the mechanism of the catalytic process. As a co-catalyst, it is worth considering the structures of the catalysts on the surface, the elementary steps of the catalytic process on the semiconductor surface, and the role of the semiconductor surface as a support in the catalytic process. The direct evidence to describe the actual catalytic process and the

evolution of the active site, coupled with the advances in theoretical calculations, is highly desirable to shed more light on the true mechanistic picture of the catalytic processes in the advanced catalysis field. In a nutshell, research on MXene is a burgeoning area but still needs much more attention under the framework of 2D nanomaterials.

Acknowledgments

The authors gratefully acknowledge funding from the Singapore Ministry of Education Academic Research Funds Tier 2 (MOE2014-T2-2-074; ARC16/15) and Tier 1 (2015-T1-001-023; RG7/15), and the GlaxoSmithKline – Economic Development Board (GSK-EDB) Trust Fund. We also acknowledge the financial support provided by the Foundation for Innovative Research Groups of the National Natural Science Foundation of China (No. 51521006) and the Projects of the National Nature Science Foundation of China (No. 51739004、21776066、51708195).

Received: ((will be filled in by the editorial staff))
Revised: ((will be filled in by the editorial staff))
Published online: ((will be filled in by the editorial staff))

References

[1] F. Bonaccorso, L. Colombo, G. H. Yu, M. Stoller, V. Tozzini, A. C. Ferrari, R. S. Ruoff and V. Pellegrini, *Science*, 2015, **347**, 1246501.

[2] Z. W. Seh, J. Kibsgaard, C. F. Dickens, I. B. Chorkendorff, J. K. Norskov and T. F. Jaramillo, *Science*, 2017, **355**, eaad4998.

[3] E. Romero, V. I. Novoderezhkin and R. van Grondelle, *Nature*, 2017, **543**, 355-365.

[4] K. S. Novoselov, A. Mishchenko, A. Carvalho and A. H. C. Neto, *Science*, 2016, **353**, aac9439.

[5] X. K. Kong, Q. C. Liu, C. L. Zhang, Z. M. Peng and Q. W. Chen, *Chem. Soc. Rev.*, 2017, **46**, 2127-2157.

[6] Q. Fu and X. H. Bao, *Chem. Soc. Rev.*, 2017, **46**, 1842-1874.

[7] C. Tan, X. Cao, X.-J. Wu, Q. He, J. Yang, X. Zhang, J. Chen, W. Zhao, S. Han, G.-H. Nam, M. Sindoro and H. Zhang, *Chem. Rev.*, 2017, **117**, 6225-6331.

[8] W. Lei, G. Liu, J. Zhang and M. Liu, *Chem. Soc. Rev.*, 2017, **46**, 3492-3509.

[9] J. Zhao, H. Liu, Z. Yu, R. Quhe, S. Zhou, Y. Wang, C. C. Liu, H. Zhong, N. Han, J. Lu, Y. Yao and K. Wu, *Prog. Mater. Sci.*, 2016, **83**, 24-151.

[10] L. Zhang, P. Bampoulis, A. N. Rudenko, Q. Yao, A. van Houselt, B. Poelsema, M. I. Katsnelson and H. J. W. Zandvliet, *Phys. Rev. Lett.*, 2016, **116**, 256804.

[11] A. Carvalho, M. Wang, X. Zhu, A. S. Rodin, H. Su and A. H. Castro Neto, *Nat. Rev. Mater.*, 2016, **1**, 16061.

[12] B. Feng, O. Sugino, R.-Y. Liu, J. Zhang, R. Yukawa, M. Kawamura, T. Iimori, H. Kim, Y. Hasegawa, H. Li, L. Chen, K. Wu, H. Kumigashira, F. Komori, T.-C. Chiang, S. Meng and I. Matsuda, *Phys. Rev. Lett.*, 2017, **118**, 096401.

[13] A. G. Kelly, T. Hallam, C. Backes, A. Harvey, A. S. Esmaeily, I. Godwin, J. Coelho, V. Nicolosi, J. Lauth, A. Kulkarni, S. Kinge, L. D. A. Siebbeles, G. S. Duesberg and J. N. Coleman, *Science*, 2017, **356**, 69-73.

[14] J. Gong and X. Bao, *Chem. Soc. Rev.*, 2017, **46**, 1770-1771.

[15] X. Duan, C. Wang, A. Pan, R. Yu and X. Duan, *Chem. Soc. Rev.*, 2015, **44**, 8859-8876.

[16] M. Chhowalla, Z. Liu and H. Zhang, *Chem. Soc. Rev.*, 2015, **44**, 2584-2586.

[17] W.-J. Ong, L.-L. Tan, Y. H. Ng, S.-T. Yong and S.-P. Chai, *Chem. Rev.*, 2016, **116**, 7159-7329.

[18] H. Yin and Z. Tang, *Chem. Soc. Rev.*, 2016, **45**, 4873-4891.

[19] V. Nicolosi, M. Chhowalla, M. G. Kanatzidis, M. S. Strano and J. N. Coleman, *Science*, 2013, **340**.

[20] H. Zhang, *ACS Nano*, 2015, **9**, 9451-9469.

[21] M. Naguib, V. N. Mochalin, M. W. Barsoum and Y. Gogotsi, *Adv. Mater.*, 2014, **26**, 992-1005.

[22] B. Anasori, M. R. Lukatskaya and Y. Gogotsi, *Nat. Rev. Mater.*, 2017, **2**, 16098.

[23] B. Aïssa, A. Ali, K. A. Mahmoud, T. Haddad and M. Nedil, *Appl. Phys. Lett.*, 2016, **109**, 043109.

[24] C. Shi, M. Beidaghi, M. Naguib, O. Mashtalir, Y. Gogotsi and S. J. Billinge, *Phys. Rev. Lett.*, 2014, **112**, 125501.

[25] M. Khazaei, A. Ranjbar, M. Arai, T. Sasaki and S. Yunoki, *J. Mater. Chem. C*, 2017, **5**, 2488-2503.

[26] X. Zhang, X. Zhao, D. Wu, Y. Jing and Z. Zhou, *Nanoscale*, 2015, **7**, 16020-16025.

[27] J. Halim, M. R. Lukatskaya, K. M. Cook, J. Lu, C. R. Smith, L. A. Naslund, S. J. May, L. Hultman, Y. Gogotsi, P. Eklund and M. W. Barsoum, *Chem. Mater.*, 2014, **26**, 2374-2381.

[28] V. N. Borysiuk, V. N. Mochalin and Y. Gogotsi, *Nanotechnology*, 2015, **26**, 265705.

[29] X.-H. Zha, J. Yin, Y. Zhou, Q. Huang, K. Luo, J. Lang, J. S. Francisco, J. He and S. Du, *J. Phys. Chem. C.*, 2016, **120**, 15082-15088.

[30] H. Kumar, N. C. Frey, L. Dong, B. Anasori, Y. Gogotsi and V. B. Shenoy, *ACS Nano*, 2017, **11**, 7648–7655.

[31] C. Chen, X. Ji, K. Xu, B. Zhang, L. Miao and J. Jiang, *ChemPhysChem*, 2017, **18**, 1897-1902.

[32] S. A. Shah, T. Habib, H. Gao, P. Gao, W. Sun, M. J. Green and M. Radovic, *Chem. Commun.*, 2016, **53**, 400-403.

[33] M. Naguib, M. Kurtoglu, V. Presser, J. Lu, J. Niu, M. Heon, L. Hultman, Y. Gogotsi

and M. W. Barsoum, *Adv. Mater.*, 2011, **23**, 4248-4253.

[34] C. Xu, L. Wang, Z. Liu, L. Chen, J. Guo, N. Kang, X. L. Ma, H. M. Cheng and W. Ren, *Nat. Mater.*, 2015, **14**, 1135-1141.

[35] Y. Gogotsi, *Nat. Mater.*, 2015, **14**, 1079-1080.

[36] G. Zou, Z. Zhang, J. Guo, B. Liu, Q. Zhang, C. Fernandez and Q. Peng, *ACS Appl. Mater. Inter.*, 2016, **8**, 22280-22286.

[37] H. Zhang, H. Dong, X. Zhang, Y. Xu and J. Fransaer, *Electrochim. Acta*, 2016, **202**, 24-31.

[38] C. J. Zhang, S. J. Kim, M. Ghidiu, M.-Q. Zhao, M. W. Barsoum, V. Nicolosi and Y. Gogotsi, *Adv. Funct. Mater.*, 2016, **26**, 4143-4151.

[39] H. Li, Y. Hou, F. Wang, M. R. Lohe, X. Zhuang, L. Niu and X. Feng, *Adv. Energy Mater.*, 2017, **7**, 1601847.

[40] M.-Q. Zhao, M. Torelli, C. E. Ren, M. Ghidiu, Z. Ling, B. Anasori, M. W. Barsoum and Y. Gogotsi, *Nano Energy*, 2016, **30**, 603-613.

[41] J. Ran, G. Gao, F. T. Li, T. Y. Ma, A. Du and S. Z. Qiao, *Nat. Commun.*, 2017, **8**, 13907.

[42] Q. Peng, J. Guo, Q. Zhang, J. Xiang, B. Liu, A. Zhou, R. Liu and Y. Tian, *J. Am. Chem. Soc.*, 2014, **136**, 4113-4116.

[43] A. K. Fard, G. McKay, R. Chamoun, T. Rhadfi, H. Preud'Homme and M. A. Atieh, *Chem. Eng. J.*, 2017, **317**, 331-342.

[44] Q. Zhang, J. Teng, G. Zou, Q. Peng, Q. Du, T. Jiao and J. Xiang, *Nanoscale*, 2016, **8**, 7085-7093.

[45] L. Ding, Y. Wei, Y. Wang, H. Chen, J. Caro and H. Wang, *Angew. Chem. Int. Ed. Engl.*, 2017, **56**, 1825-1829.

[46] L. Lorencova, T. Bertok, E. Dosekova, A. Holazova, D. Paprckova, A. Vikartovska, V. Sasinkova, J. Filip, P. Kasak, M. Jerigova, D. Velic, K. A. Mahmoud and J. Tkac, *Electrochim. Acta*, 2017, **235**, 471-479.

[47] B. Xu, M. Zhu, W. Zhang, X. Zhen, Z. Pei, Q. Xue, C. Zhi and P. Shi, *Adv. Mater.*, 2016, **28**, 3333-3339.

[48] R. Li, L. Zhang, L. Shi and P. Wang, *ACS Nano*, 2017, **11**, 3752-3759.

[49] H. Lin, X. Wang, L. Yu, Y. Chen and J. Shi, *Nano Lett.*, 2017, **17**, 384-391.

[50] Q. Xue, H. Zhang, M. Zhu, Z. Pei, H. Li, Z. Wang, Y. Huang, Y. Huang, Q. Deng, J. Zhou, S. Du, Q. Huang and C. Zhi, *Adv. Mater.*, 2017, **29**, 1604847.

[51] J.-C. Lei, X. Zhang and Z. Zhou, *Front. Phys.*, 2015, **10**, 276-286.

[52] P. Kumar, H. Abuhimd, W. Wahyudi, M. Li, J. Ming and L.-J. Li, *ECS J. Solid. State. Sci. Technol.*, 2016, **5**, Q3021-Q3025.

[53] Y. Yoon, K. Lee and H. Lee, *Nanotechnology*, 2016, **27**, 172001.

[54] L. Dong, H. Kumar, B. Anasori, Y. Gogotsi and V. B. Shenoy, *J. Phys. Chem. Lett.*, 2017, **8**, 422-428.

[55] V. M. Hong Ng, H. Huang, K. Zhou, P. S. Lee, W. Que, J. Z. Xu and L. B. Kong, *J. Mater. Chem. A*, 2017, **5**, 3039-3068.

[56] K. Wang, Y. Zhou, W. Xu, D. Huang, Z. Wang and M. Hong, *Ceram. Int.*, 2016, **42**, 8419-8424.

[57] L. Zhou, F. Wu, J. Yu, Q. Deng, F. Zhang and G. Wang, *Carbon*, 2017, **118**, 50-57.

[58] M. R. Lukatskaya, O. Mashtalir, C. E. Ren, Y. Dall'Agnese, P. Rozier, P. L. Taberna, M. Naguib, P. Simon, M. W. Barsoum and Y. Gogotsi, *Science*, 2013, **341**, 1502-1505.

[59] Z. Guo, J. Zhou, L. Zhu and Z. Sun, *J. Mater. Chem. A*, 2016, **4**, 11446-11452.

[60] H. Zhang, G. Yang, X. Zuo, H. Tang, Q. Yang and G. Li, *J. Mater. Chem. A.*, 2016, **4**, 12913-12920.

[61] L. Zhao, B. Dong, S. Li, L. Zhou, L. Lai, Z. Wang, S. Zhao, M. Han, K. Gao, M. Lu, X. Xie, B. Chen, Z. Liu, X. Wang, H. Zhang, H. Li, J. Liu, H. Zhang, X. Huang, and W. Huang. *ACS Nano*, 2017, **11**, 5800–5807.

[62] M. Khazaei, A. Ranjbar, M. Arai, T. Sasaki and S. Yunoki. *J. Mater. Chem. C.*, 2017, **5**, 2488-2503.

[63] Q. Tang, Z. Zhou and P. Shen, *J. Am. Chem. Soc.*, 2012, **134**, 16909-16916.

[64] J. Yang, X. Zhou, X. Luo, S. Zhang and L. Chen, *Appl. Phys. Lett.*, 2016, **109**, 203109.

[65] Y. Zhou, K. Luo, X. Zha, Z. Liu, X. Bai, Q. Huang, Z. Guo, C.-T. Lin and S. Du, *J. Phys. Chem. C*, 2016, **120**, 17143-17152.

[66] X. H. Zha, Q. Huang, J. He, H. He, J. Zhai, J. S. Francisco and S. Du, *Sci. Rep.*, 2016, **6**, 27971.

[67] M. Khazaei, M. Arai, T. Sasaki, C.-Y. Chung, N. S. Venkataramanan, M. Estili, Y. Sakka and Y. Kawazoe, *Adv. Funct. Mater.*, 2013, **23**, 2185-2192.

[68] X. H. Zha, J. Zhou, Y. Zhou, Q. Huang, J. He, J. S. Francisco, K. Luo and S. Du, *Nanoscale*, 2016, **8**, 6110-6117.

[69] A. Miranda, J. Halim, M. W. Barsoum and A. Lorke, *Appl. Phys. Lett.*, 2016, **108**, 033102.

[70] A. Lipatov, M. Alhabeb, M. R. Lukatskaya, A. Boson, Y. Gogotsi and A. Sinitskii, *Adv. Electron. Mater.*, 2016, **2**, 1600255.

[71] F. Shahzad, M. Alhabeb, C. B. Hatter, B. Anasori, S. M. Hong, C. M. Koo and Y. Gogotsi, *Science*, 2016, **353**, 1137-1140.

[72] H. Wang, Y. Wu, J. Zhang, G. Li, H. Huang, X. Zhang and Q. Jiang, *Mater. Lett.*, 2015, **160**, 537-540.

[73] X. Sang, Y. Xie, M. W. Lin, M. Alhabeb, K. L. Van Aken, Y. Gogotsi, P. R. Kent, K. Xiao and R. R. Unocic, *ACS Nano*, 2016, **10**, 9193-9200.

[74] J. Yang, X. Luo, S. Zhang and L. Chen, *Phys. Chem. Chem. Phys.*, 2016, **18**, 12914-12919.

[75] L. Li, *J. Phys. Chem. C.*, 2016, **120**, 24857-24865.

[76] F. M. Römer, U. Wiedwald, T. Strusch, J. Halim, E. Mayerberger, M. W. Barsoum and M. Farle, *RSC Adv.*, 2017, **7**, 13097-13103.

[77] Y. Yang, S. Umrao, S. Lai and S. Lee, *J. Phys. Chem. Lett.*, 2017, **8**, 859-865.

[78] S. Lai, J. Jeon, S. K. Jang, J. Xu, Y. J. Choi, J. H. Park, E. Hwang and S. Lee, *Nanoscale*, 2015, **7**, 19390-19396.

[79] L. Li, Comput. Mater. Sci., 2016, **124**, 8-14.

[80] Y. Lee, S. B. Cho and Y. C. Chung, *ACS Appl. Mater. Inter.*, 2014, **6**, 14724-14728.

[81] X.-f. Yu, J.-b. Cheng, Z.-b. Liu, Q.-z. Li, W.-z. Li, X. Yang and B. Xiao, *RSC Adv.*, 2015, **5**, 30438-30444.

[82] Z. Ma, Z. Hu, X. Zhao, Q. Tang, D. Wu, Z. Zhou and L. Zhang, *J. Phys. Chem. C.*,

2014, **118**, 5593-5599.

[83] X. Li, Y. Dai, Y. Ma, Q. Liu and B. Huang, *Nanotechnology*, 2015, **26**, 135703.

[84] B. Anasori, C. Shi, E. J. Moon, Y. Xie, C. A. Voigt, P. R. C. Kent, S. J. May, S. J. L. Billinge, M. W. Barsoum and Y. Gogotsi. *Nanoscale Horiz.*, 2016, **1**, 227-234.

[85] L. Dong, H. Kumar, B. Anasori, Y. Gogotsi and V. B. Shenoy. *J. Phys. Chem. Lett.*, 2017, **8**, 422-428.

[86] D. Magne, V. Mauchamp, S. Célérier, P. Chartier and T. Cabioc'h, *Phy. Rev. B.*, 2015, **91**.

[87] G. R. Berdiyorov and M. E. Madjet, *Appl. Surf. Sci.*, 2016, **390**, 1009-1014.

[88] G. R. Berdiyorov, *AIP Adv.*, 2016, **6**, 055105.

[89] K. Hantanasirisakul, M.-Q. Zhao, P. Urbankowski, J. Halim, B. Anasori, S. Kota, C. E. Ren, M. W. Barsoum and Y. Gogotsi, *Adv. Electron. Mater.*, 2016, **2**, 1600050.

[90] A. D. Dillon, M. J. Ghidiu, A. L. Krick, J. Griggs, S. J. May, Y. Gogotsi, M. W. Barsoum and A. T. Fafarman, *Adv. Funct. Mater.*, 2016, **26**, 4162-4168.

[91] Z. Guo, N. Miao, J. Zhou, B. Sa and Z. Sun, *J. Mater. Chem. C*, 2017, **5**, 978-984.

[92] C. Peng, H. Wang, H. Yu and F. Peng, *Mater. Res. Bull.*, 2017, **89**, 16-25.

[93] U. Yorulmaz, A. Ozden, N. K. Perkgoz, F. Ay and C. Sevik, *Nanotechnology*, 2016, **27**, 335702.

[94] Z. Guo, J. Zhou, C. Si and Z. Sun, *Phys. Chem. Chem. Phys.*, 2015, **17**, 15348-15354.

[95] Y. Bai, K. Zhou, N. Srikanth, J. H. L. Pang, X. He and R. Wang, *RSC Adv.*, 2016, **6**, 35731-35739.

[96] J. Come, Y. Xie, M. Naguib, S. Jesse, S. V. Kalinin, Y. Gogotsi, P. R. C. Kent and N. Balke, *Adv. Energy Mater.*, 2016, **6**, 1502290.

[97] H. Zhang, L. Wang, Q. Chen, P. Li, A. Zhou, X. Cao and Q. Hu, *Mater. Des.*, 2016, **92**, 682-689.

[98] C. Hu, F. Shen, D. Zhu, H. Zhang, J. Xue and X. Han, *Front. Energy Res.*, 2017, **4**, DOI: 10.3389/fenrg.2016.00041.

[99] X. H. Zha, Q. Huang, J. He, H. M. He, J. Y. Zhai, J. S. Francisco and S. Y. Du, Sci. *Rep.*, 2016, **6**, 27971.

[100] X.-H. Zha, J. Zhou, Y. Zhou, Q. Huang, J. He, J. S. Francisco, K. Luo and S. Du, Nanoscale, 2016, **8**, 6110-6117.

[101] L.-Y. Gan, D. Huang and U. Schwingenschlögl, *J. Mater. Chem. A.*, 2013, **1**, 13672.

[102] R. B. Rakhi, B. Ahmed, M. N. Hedhili, D. H. Anjum and H. N. Alshareef, *Chem.* Mater., 2015, **27**, 5314-5323.

[103] Z. Li, L. Wang, D. Sun, Y. Zhang, B. Liu, Q. Hu and A. Zhou, *Mater. Sci. Eng. B*, 2015, **191**, 33-40.

[104] J. Li, Y. Du, C. Huo, S. Wang and C. Cui, *Ceram. Int.*, 2015, **41**, 2631-2635.

[105] H. Ghassemi, W. Harlow, O. Mashtalir, M. Beidaghi, M. R. Lukatskaya, Y. Gogotsi and M. L. Taheri, *J. Mater. Chem. A.*, 2014, **2**, 14339.

[106] M. Naguib, O. Mashtalir, J. Carle, V. Presser, J. Lu, L. Hultman, Y. Gogotsi and M. W. Barsoum, *ACS Nano*, 2012, **6**, 1322-1331.

[107] A. Feng, Y. Yu, Y. Wang, F. Jiang, Y. Yu, L. Mi and L. Song, *Mater. Des.*, 2017, **114**, 161-166.

[108] M. Ghidiu, M. R. Lukatskaya, M. Q. Zhao, Y. Gogotsi and M. W. Barsoum, Nature, 2014, **516**, 78-81.

[109] P. Urbankowski, B. Anasori, T. Makaryan, D. Er, S. Kota, P. L. Walsh, M. Zhao, V. B. Shenoy, M. W. Barsoum and Y. Gogotsi, *Nanoscale*, 2016, **8**, 11385-11391.

[110] D. Sun, M. Wang, Z. Li, G. Fan, L.-Z. Fan and A. Zhou, *Electrochem.* Commun., 2014, **47**, 80-83.

[111] T. Zhang, L. Pan, H. Tang, F. Du, Y. Guo, T. Qiu and J. Yang, *J. Alloys* Compd., 2017, **695**, 818-826.

[112] L. Wang, H. Zhang, B. Wang, C. Shen, C. Zhang, Q. Hu, A. Zhou and B. Liu, Electron. *Mater. Lett.*, 2016, **12**, 702-710.

[113] M. A. Hope, A. C. Forse, K. J. Griffith, M. R. Lukatskaya, M. Ghidiu, Y. Gogotsi and C. P. Grey, *Phys. Chem. Chem. Phys.*, 2016, **18**, 5099-5102.

[114] J. Halim, K. M. Cook, M. Naguib, P. Eklund, Y. Gogotsi, J. Rosen and M. W. Barsoum, *Appl. Surf. Sci.*, 2016, **362**, 406-417.

[115] J. Zhou, X. Zha, X. Zhou, F. Chen, G. Gao, S. Wang, C. Shen, T. Chen, C. Zhi, P.

Eklund, S. Du, J. Xue, W. Shi, Z. Chai and Q. Huang, *ACS Nano*, 2017, **11**, 3841-3850.

[116] Q. Tao, M. Dahlqvist, J. Lu, S. Kota, R. Meshkian, J. Halim, J. Palisaitis, L. Hultman, M. W. Barsoum, P. O. A. Persson and J. Rosen, *Nat. Commun.*, 2017, **8**, 14949.

[117] A. Vaughn, J. Ball, T. Heil, D. J. Morgan, G. I. Lampronti, G. Maršalkaitė, C. L. Raston, N. P. Power and S. Kellici, *Chem. Eur. J.*, 2017, **23**, 1-7.

[118] J. Halim, S. Kota, M. R. Lukatskaya, M. Naguib, M.-Q. Zhao, E. J. Moon, J. Pitock, J. Nanda, S. J. May, Y. Gogotsi and M. W. Barsoum, *Adv. Funct. Mater.*, 2016, **26**, 3118-3127.

[119] R. Meshkian, L.-Å. Näslund, J. Halim, J. Lu, M. W. Barsoum and J. Rosen, *Scr.* Mater., 2015, **108**, 147-150.

[120] M. Q. Zhao, X. Xie, C. E. Ren, T. Makaryan, B. Anasori, G. Wang and Y. Gogotsi, *Adv. Mater.*, 2017, DOI: 10.1002/adma.201702410.

[121] O. Mashtalir, M. R. Lukatskaya, M. Q. Zhao, M. W. Barsoum and Y. Gogotsi, Adv. *Mater.*, 2015, **27**, 3501-3506.

[122] O. Mashtalir, M. R. Lukatskaya, A. I. Kolesnikov, E. Raymundo-Pinero, M. Naguib, M. W. Barsoum and Y. Gogotsi, *Nanoscale*, 2016, **8**, 9128-9133.

[123] H. Wang, J. Zhang, Y. Wu, H. Huang, G. Li, X. Zhang and Z. Wang, *Appl. Surf. Sci.*, 2016, **384**, 287-293.

[124] L. Hao, H. Zhang, X. Wu, J. Zhang, J. Wang and Y. Li, *Part A Appl. Sci.* Manuf., 2017, **100**, 139-149.

[125] J. Luo, W. Zhang, H. Yuan, C. Jin, L. Zhang, H. Huang, C. Liang, Y. Xia, J. Zhang, Y. Gan and X. Tao, *ACS Nano*, 2017, **11**, 2459-2469.

[126] J. Luo, X. Tao, J. Zhang, Y. Xia, H. Huang, L. Zhang, Y. Gan, C. Liang and W. Zhang, *ACS Nano*, 2016, **10**, 2491-2499.

[127] D. Geng, X. Zhao, Z. Chen, W. Sun, W. Fu, J. Chen, W. Liu, W. Zhou and K. P. Loh, *Adv. Mater.*, 2017, DOI: 10.1002/adma.201700072.

[128] X. Xie, S. Chen, W. Ding, Y. Nie and Z. Wei, *Chem. Commun.*, 2013, **49**, 10112-10114.

[129] X. Li, C. Zeng and G. Fan, *Int. J. Hydrogen Energy*, 2015, **40**, 9217-9224.

[130] E. Satheeshkumar, T. Makaryan, A. Melikyan, H. Minassian, Y. Gogotsi and M. Yoshimura, *Sci. Rep.*, 2016, **6**, 32049.

[131] Z. Zhang, H. Li, G. Zou, C. Fernandez, B. Liu, Q. Zhang, J. Hu and Q. Peng, ACS *Sustain. Chem. Eng.*, 2016, **4**, 6763-6771.

[132] M. Ming, Y. Ren, M. Hu, Y. Zhang, T. Sun, Y. Ma, X. Li, W. Jiang, D. Gao, J. Bi and G. Fan, *Appl Catal B: Environ*, 2017, **210**, 462-469.

[133] R. B. Rakhi, P. Nayuk, C. Xia and H. N. Alshareef, *Sci. Rep.*, 2016, **6**, 36422.

[134] Y. Gao, L. Wang, Z. Li, A. Zhou, Q. Hu and X. Cao, *Solid State Sci.*, 2014, **35**, 62-65.

[135] Y. Gao, L. Wang, A. Zhou, Z. Li, J. Chen, H. Bala, Q. Hu and X. Cao, *Mater.* Lett., 2015, **150**, 62-64.

[136] F. Wang, Z. Wang, J. Zhu, H. Yang, X. Chen, L. Wang and C. Yang, *J. Mater. Sci.*, 2017, **52**, 3556-3565.

[137] F. Wang, C. Yang, M. Duan, Y. Tang and J. Zhu, *Biosens. Bioelectron.*, 2015, **74**, 1022-1028.

[138] J. F. Zhu, Y. Tang, C. H. Yang, F. Wang and M. J. Cao, *J. Electrochem. Soc.*, 2016, **163**, A785-A791.

[139] Y. Tang, J. Zhu, C. Yang and F. Wang, *J. Alloys Compd.*, 2016, **685**, 194-201.

[140] C. Peng, X. Yang, Y. Li, H. Yu, H. Wang and F. Peng, *ACS Appl. Mater. Inter.*, 2016, **8**, 6051-6060.

[141] C. Zhang, M. Beidaghi, M. Naguib, M. R. Lukatskaya, M.-Q. Zhao, B. Dyatkin, K. M. Cook, S. J. Kim, B. Eng, X. Xiao, D. Long, W. Qiao, B. Dunn and Y. Gogotsi, *Chem. Mater.*, 2016, **28**, 3937-3943.

[142] J. Zhu, X. Lu and L. Wang, *RSC Adv.*, 2016, **6**, 98506-98513.

[143] F. Wang, M. Cao, Y. Qin, J. Zhu, L. Wang and Y. Tang, *RSC Adv.*, 2016, **6**, 88934-88942.

[144] Q. X. Xia, J. Fu, J. M. Yun, R. S. Mane and K. H. Kim, *RSC Adv.*, 2017, **7**, 11000-11011.

[145] Y. Wang, H. Dou, J. Wang, B. Ding, Y. Xu, Z. Chang and X. Hao, *J. Power* Sources,

2016, **327**, 221-228.

[146] Y. Wu, P. Nie, J. Jiang, B. Ding, H. Dou and X. Zhang, *ChemElectroChem*, 2017, **4**, 1560-1565.

[147] X. Wu, Z. Wang, M. Yu, L. Xiu and J. Qiu, *Adv. Mater.*, 2017.

[148] Y. Lu, M. Yao, A. Zhou, Q. Hu and L. Wang, *J. Nanomater.*, 2017, **2017**, 1-5.

[149] M. Boota, M. Pasini, F. Galeotti, W. Porzio, M.-Q. Zhao, J. Halim and Y. Gogotsi, *Chem. Mater.*, 2017, **29**, 2731-2738.

[150] M. Naguib, T. Saito, S. Lai, M. S. Rager, T. Aytug, M. Parans Paranthaman, M.-Q. Zhao and Y. Gogotsi, *RSC Adv.*, 2016, **6**, 72069-72073.

[151] Z. Huang, S. Wang, S. Kota, Q. Pan, M. W. Barsoum and C. Y. Li, *Polymer*, 2016, **102**, 119-126.

[152] Z. Ling, C. E. Ren, M. Q. Zhao, J. Yang, J. M. Giammarco, J. S. Qiu, M. W. Barsoum and Y. Gogotsi, *Proc. Natl. Acad. Sci.*, 2014, **111**, 16676-16681.

[153] E. A. Mayerberger, O. Urbanek, R. M. McDaniel, R. M. Street, M. W. Barsoum and C. L. Schauer, *J. Appl. Polym. Sci.*, 2017, **134**, 45295.

[154] C. Chen, M. Boota, X. Xie, M. Zhao, B. Anasori, C. E. Ren, L. Miao, J. Jiang and Y. Gogotsi, *J. Mater. Chem. A*, 2017, **5**, 5260-5265.

[155] M. Boota, B. Anasori, C. Voigt, M. Q. Zhao, M. W. Barsoum and Y. Gogotsi, Adv. *Mater.*, 2016, **28**, 1517-1522.

[156] M. Zhu, Y. Huang, Q. Deng, J. Zhou, Z. Pei, Q. Xue, Y. Huang, Z. Wang, H. Li, Q. Huang and C. Zhi, *Adv. Energy Mater.*, 2016, **6**, 1600969.

[157] J. Chen, K. Chen, D. Tong, Y. Huang, J. Zhang, J. Xue, Q. Huang and T. Chen, Chem. *Commun.*, 2015, **51**, 314-317.

[158] K. Maleski, V. N. Mochalin and Y. Gogotsi, *Chem. Mater.*, 2017, **29**, 1632-1640.

[159] P. Yan, R. Zhang, J. Jia, C. Wu, A. Zhou, J. Xu and X. Zhang, *J. Power Sources*, 2015, **284**, 38-43.

[160] M. Q. Zhao, C. E. Ren, Z. Ling, M. R. Lukatskaya, C. Zhang, K. L. Van Aken, M. W. Barsoum and Y. Gogotsi, *Adv. Mater.*, 2015, **27**, 339-345.

[161] Y. Dall'Agnese, P. Rozier, P.-L. Taberna, Y. Gogotsi and P. Simon, *J. Power*

Sources, 2016, **306**, 510-515.

[162] A. Byeon, A. M. Glushenkov, B. Anasori, P. Urbankowski, J. Li, B. W. Byles, B. Blake, K. L. Van Aken, S. Kota, E. Pomerantseva, J. W. Lee, Y. Chen and Y. Gogotsi, *J. Power Sources*, 2016, **326**, 686-694.

[163] X. Xie, M.-Q. Zhao, B. Anasori, K. Maleski, C. E. Ren, J. Li, B. W. Byles, E. Pomerantseva, G. Wang and Y. Gogotsi, *Nano Energy*, 2016, **26**, 513-523.

[164] X. Liang, Y. Rangom, C. Y. Kwok, Q. Pang and L. F. Nazar, *Adv. Mater.*, 2017, **29**, 1603040.

[165] C. Zhao, Q. Wang, H. Zhang, S. Passerini and X. Qian, *ACS Appl. Mater. Inter.*, 2016, **8**, 15661-15667.

[166] T. Y. Ma, J. L. Cao, M. Jaroniec and S. Z. Qiao, *Angew. Chem. Int. Ed. Engl.*, 2016, **55**, 1138-1142.

[167] Z. Lin, D. Sun, Q. Huang, J. Yang, M. W. Barsoum and X. Yan, *J. Mater.* Chem. *A*, 2015, **3**, 14096-14100.

[168] L. Yang, X. Li, S. He, G. Du, X. Yu, J. Liu, Q. Gao, R. Hu and M. Zhu, *J.* Mater. *Chem. A*, 2016, **4**, 10842-10849.

[169] H. Liu, C. Duan, C. Yang, W. Shen, F. Wang and Z. Zhu, *Sens. Actuators B* Chem., 2015, **218**, 60-66.

[170] F. Bonaccorso, L. Colombo, G. H. Yu, M. Stoller, V. Tozzini, A. C. Ferrari, R. S. Ruoff and V. Pellegrini, *Science*, 2015, **347**, 10.

[171] H. Wang, X. Yuan, G. Zeng, Y. Wu, Y. Liu, Q. Jiang and S. Gu, *Adv. Colloid* Inter. *Sci.*, 2015, **221**, 41-59.

[172] J. Zhou, H. Shen, Z. Li, S. Zhang, Y. Zhao, X. Bi, Y. Wang, H. Cui and S. Zhuo, Electrochim. *Acta*, 2016, **209**, 557-564.

[173] J. Zhou, T. Zhu, W. Xing, Z. Li, H. Shen and S. Zhuo, *Electrochim. Acta*, 2015, **160**, 152-159.

[174] L. Jiang, X. Yuan, J. Liang, J. Zhang, H. Wang and G. Zeng, *J. Power Sources*, 2016, **331**, 408-425.

[175] M. R. Lukatskaya, S.-M. Bak, X. Yu, X.-Q. Yang, M. W. Barsoum and Y. Gogotsi,

Adv. Energy Mater., 2015, **5**, 1500589.

[176] M. D. Levi, M. R. Lukatskaya, S. Sigalov, M. Beidaghi, N. Shpigel, L. Daikhin, D. Aurbach, M. W. Barsoum and Y. Gogotsi, *Adv. Energy Mater.*, 2015, **5**, 1400815.

[177] M. Hu, Z. Li, T. Hu, S. Zhu, C. Zhang and X. Wang, *ACS Nano*, 2016, **10**, 11344-11350.

[178] X. Ji, K. Xu, C. Chen, B. Zhang, Y. Ruan, J. Liu, L. Miao and J. Jiang, *Phys.* Chem. *Chem. Phys.*, 2016, **18**, 4460-4467.

[179] Z. Lin, D. Barbara, P.-L. Taberna, K. L. Van Aken, B. Anasori, Y. Gogotsi and P. Simon, *J. Power Sources*, 2016, **326**, 575-579.

[180] Z. Lin, P. Rozier, B. Duployer, P.-L. Taberna, B. Anasori, Y. Gogotsi and P. Simon, *Electrochem. Commun.*, 2016, **72**, 50-53.

[181] M. R. Lukatskaya, S. Kota, Z. Lin, M.-Q. Zhao, N. Shpigel, M. D. Levi, J. Halim, P.-L. Taberna, M. W. Barsoum, P. Simon and Y. Gogotsi, *Nature Energy*, 2017, **6**, 17105.

[182] Y. Tang, J. Zhu, C. Yang and F. Wang, *J. Electrochem. Soc.*, 2016, **163**, A1975-A1982.

[183] Y. Dall'Agnese, M. R. Lukatskaya, K. M. Cook, P.-L. Taberna, Y. Gogotsi and P. Simon, *Electrochem. Commun.*, 2014, **48**, 118-122.

[184] R. B. Rakhi, B. Ahmed, M. N. Hedhili, D. H. Anjum and H. N. Alshareef, Chem. *Mater.*, 2015, **27**, 5314-5323.

[185] C. Yang, W. Que, X. Yin, Y. Tian, Y. Yang and M. Que, *Electrochim. Acta*, 2017, **225**, 416-424.

[186] X. Lu, J. Zhu, W. Wu and B. Zhang, *Electrochim. Acta*, 2017, **228**, 282-289.

[187] J. Yan, C. E. Ren, K. Maleski, C. B. Hatter, B. Anasori, P. Urbankowski, A. Sarycheva and Y. Gogotsi, *Adv. Funct. Mater.*, 2017, DOI: 10.1002/adfm.201701264.

[188] B.-S. Shen, H. Wang, L.-J. Wu, R.-S. Guo, Q. Huang and X.-B. Yan, *Chin.* Chem. *Lett.*, 2016, **27**, 1586-1591.

[189] Y.-Y. Peng, B. Akuzum, N. Kurra, M.-Q. Zhao, M. Alhabeb, B. Anasori, E. C. Kumbur, H. N. Alshareef, M.-D. Ger and Y. Gogotsi, *Energy Environ. Sci.*, 2016, **9**,

2847-2854.

[190] C. J. Zhang, B. Anasori, A. Seral-Ascaso, S. H. Park, N. McEvoy, A. Shmeliov, G. S. Duesberg, J. N. Coleman, Y. Gogotsi and V. Nicolosi, *Adv. Mater.*, 2017.

[191] M. Hu, Z. Li, H. Zhang, T. Hu, C. Zhang, Z. Wu and X. Wang, *Chem.* Commun., 2015, **51**, 13531-13533.

[192] S.-Y. Lin and X. Zhang, *J. Power Sources*, 2015, **294**, 354-359.

[193] Q. Fu, J. Wen, N. Zhang, L. Wu, M. Zhang, S. Lin, H. Gao and X. Zhang, *RSC Adv.*, 2017, **7**, 11998-12005.

[194] D. Er, J. Li, M. Naguib, Y. Gogotsi and V. B. Shenoy, *ACS Appl. Mater. Inter.*, 2014, **6**, 11173-11179.

[195] X. Lv, W. Wei, Q. Sun, L. Yu, B. Huang and Y. Dai, *Chemphyschem*, 2017, **18**, 1627-1634.

[196] Y. Zhou and X. Zu, *Electrochim. Acta*, 2017, **235**, 167-174.

[197] M. Naguib, J. Come, B. Dyatkin, V. Presser, P.-L. Taberna, P. Simon, M. W. Barsoum and Y. Gogotsi, *Electrochem. Commun.*, 2012, **16**, 61-64.

[198] Y. Xie, M. Naguib, V. N. Mochalin, M. W. Barsoum, Y. Gogotsi, X. Yu, K. W. Nam, X. Q. Yang, A. I. Kolesnikov and P. R. Kent, *J. Am. Chem. Soc.*, 2014, **136**, 6385-6394.

[199] S. Zhao, W. Kang and J. Xue, *J. Phy. Chem. C*, 2014, **118**, 14983-14990.

[200] G. R. Berdiyorov, *Appl. Surf. Sci.*, 2015, **359**, 153-157.

[201] J. Come, J. M. Black, M. R. Lukatskaya, M. Naguib, M. Beidaghi, A. J. Rondinone, S. V. Kalinin, D. J. Wesolowski, Y. Gogotsi and N. Balke, *Nano Energy*, 2015, **17**, 27-35.

[202] S. J. Kim, M. Naguib, M. Zhao, C. Zhang, H.-T. Jung, M. W. Barsoum and Y. Gogotsi, *Electrochim. Acta*, 2015, **163**, 246-251.

[203] J. Zhu, A. Chroneos and U. Schwingenschlögl, *Phys. Status Solidi Rapid Res.* Lett., 2015, **9**, 726-729.

[204] B. Ahmed, D. H. Anjum, M. N. Hedhili, Y. Gogotsi and H. N. Alshareef, Nanoscale, 2016, **8**, 7580-7587.

[205] M. Ashton, R. G. Hennig and S. B. Sinnott, *Appl. Phy. Lett.*, 2016, **108**, 023901.

[206] C. E. Ren, M.-Q. Zhao, T. Makaryan, J. Halim, M. Boota, S. Kota, B. Anasori, M. W. Barsoum and Y. Gogotsi, *ChemElectroChem*, 2016, **3**, 689-693.

[207] D. Sun, Q. Hu, J. Chen, X. Zhang, L. Wang, Q. Wu and A. Zhou, *ACS Appl.* Mater. *Inter.*, 2016, **8**, 74-81.

[208] A. T. Tesfaye, O. Mashtalir, M. Naguib, M. W. Barsoum, Y. Gogotsi and T. Djenizian, *ACS Appl. Mater. Inter.s*, 2016, **8**, 16670-16676.

[209] J. Xu, M.-Q. Zhao, Y. Wang, W. Yao, C. Chen, B. Anasori, A. Sarycheva, C. E. Ren, T. Mathis, L. Gomes, L. Zhenghua and Y. Gogotsi, *ACS Energy Lett.*, 2016, **1**, 1094-1099.

[210] T. Zhao, S. Zhang, Y. Guo and Q. Wang, *Nanoscale*, 2016, **8**, 233-242.

[211] A. Byeon, M. Q. Zhao, C. E. Ren, J. Halim, S. Kota, P. Urbankowski, B. Anasori, M. W. Barsoum and Y. Gogotsi, *ACS Appl. Mater. Inter.*, 2017, **9**, 4296-4300.

[212] F. Du, H. Tang, L. Pan, T. Zhang, H. Lu, J. Xiong, J. Yang and C. Zhang, Electrochim. *Acta*, 2017, **235**, 690-699.

[213] P. Simon, *ACS Nano*, 2017, **11**, 2393-2396.

[214] C. Eames and M. S. Islam, *J. Am. Chem. Soc.*, 2014, **136**, 16270-16276.

[215] J. Zhu, A. Chroneos, J. Eppinger and U. Schwingenschlögl, *Appl. Mater. Today*, 2016, **5**, 19-24.

[216] J. Zhu and U. Schwingenschlögl, *2D Mater.*, 2017, **4**, 025073.

[217] B. Anasori, Y. Xie, M. Beidaghi, J. Lu, B. C. Hosler, L. Hultman, P. R. C. Kent, Y. Gogotsi and M. W. Barsoum, *ACS Nano*, 2015, **9**, 9507-9516.

[218] X. Zhao, M. Liu, Y. Chen, B. Hou, N. Zhang, B. Chen, N. Yang, K. Chen, J. Li and L. An, *J. Mater. Chem. A*, 2015, **3**, 7870-7876.

[219] W. Bao, X. Xie, J. Xu, X. Guo, J. Song, D. Su, G. Wang and W. Wu, *Chem.* Eur. *J*, 2017, DOI: 10.1002/chem.201702387.

[220] J. Song, D. Su, X. Xie, X. Guo, W. Bao, G. Shao and G. Wang, *ACS Appl. Mater. Inter.*, 2016, **8**, 29427-29433.

[221] X. Liang, A. Garsuch and L. F. Nazar, *Angew. Chem. Int. Ed. Engl.*, 2015, **54**,

3907-3911.

[222] E. S. Sim, G. S. Yi, M. Je, Y. Lee and Y.-C. Chung, *J. Power Sources*, 2017, **342**, 64-69.

[223] Y. Zhao and J. Zhao, *Appl. Surf. Sci.*, 2017, **412**, 591-598.

[224] Y. Dall'Agnese, P. L. Taberna, Y. Gogotsi and P. Simon, *J. Phys. Chem. Lett.*, 2015, **6**, 2305-2309.

[225] S. Kajiyama, L. Szabova, K. Sodeyama, H. Iinuma, R. Morita, K. Gotoh, Y. Tateyama, M. Okubo and A. Yamada, *ACS Nano*, 2016, **10**, 3334-3341.

[226] X. Wang, S. Kajiyama, H. Iinuma, E. Hosono, S. Oro, I. Moriguchi, M. Okubo and A. Yamada, *Nat. Commun.*, 2015, **6**, 6544.

[227] Y.-X. Yu, *J. Phys. Chem. C*, 2016, **120**, 5288-5296.

[228] Y. Xie, Y. Dall'Agnese, M. Naguib, Y. Gogotsi, M. W. Barsoum, H. L. Zhuang and P. R. C. Kent, *ACS Nano*, 2014, **8**, 9606-9615.

[229] E. Yang, H. Ji, J. Kim, H. Kim and Y. Jung, *Phys. Chem. Chem. Phys.*, 2015, **17**, 5000-5005.

[230] X. Wang, X. Shen, Y. Gao, Z. Wang, R. Yu and L. Chen, *J. Am. Chem. Soc.*, 2015, 137, 2715-2721.

[231] J. Hu, B. Xu, S. A. Yang, S. Guan, C. Ouyang and Y. Yao, *ACS Appl. Mater. Inter.*, 2015, **7**, 24016-24022.

[232] Z. Wu, X. Yuan, H. Wang, Z. Wu, L. Jiang, H. Wang, L. Zhang, Z. Xiao, X. Chen and G. Zeng, *Appl. Catal. B: Environ.*, 2017, **202**, 104-111.

[233] Y. Wu, H. Luo, X. Jiang, H. Wang and J. Geng, *RSC Adv.*, 2015, **5**, 4905-4908.

[234] H. Wang, X. Yuan, Y. Wu, G. Zeng, X. Chen, L. Leng, Z. Wu, L. Jiang and H. Li, *J. Hazard. Mater.*,, 2015, **286**, 187-194.

[235] H. Wang, X. Yuan, Y. Wu, G. Zeng, X. Chen, L. Leng and H. Li, *Appl. Catal. B:* Environ., 2015, **174-175**, 445-454.

[236] H. Wang, X. Yuan, Y. Wu, X. Chen, L. Leng and G. Zeng, *RSC Adv.*, 2015, **5**, 32531-32535.

[237] L. Jiang, X. Yuan, Y. Pan, J. Liang, G. Zeng, Z. Wu and H. Wang, *Appl. Catal. B:*

Environ., 2017, **217**, 388-406.

[238] Z. Wu, X. Yuan, J. Zhang, H. Wang, L. Jiang and G. Zeng, *ChemCatChem*, 2017, **9**, 41-64.

[239] H. Wang, X. Yuan, Y. Wu, G. Zeng, W. Tu, C. Sheng, Y. Deng, F. Chen and J. W. Chew, *Appl. Catal. B: Environ.*, 2017, **209**, 543-553.

[240] X. Yuan, H. Wang, Y. Wu, G. Zeng, X. Chen, L. Leng, Z. Wu and H. Li, *Appl.* Organomet. *Chem.*, 2016, **30**, 289-296.

[241] H. Wang, X. Yuan, Y. Wu, G. Zeng, H. Dong, X. Chen, L. Leng, Z. Wu and L. Peng, *Appl. Catal. B: Environ.*, 2016, **186**, 19-29.

[242] O. Mashtalir, K. M. Cook, V. N. Mochalin, M. Crowe, M. W. Barsoum and Y. Gogotsi, *J. Mater. Chem. A*, 2014, **2**, 14334.

[243] H. Wang, R. Peng, Z. D. Hood, M. Naguib, S. P. Adhikari and Z. Wu, ChemSusChem, 2016, **9**, 1490-1497.

[244] J. Wang, X. Ge, Z. Liu, L. Thia, Y. Yan, W. Xiao and X. Wang, *J. Am. Chem. Soc.*, 2017, **139**, 1878-1884.

[245] Y. Yan, L. Thia, B. Y. Xia, X. Ge, Z. Liu, A. Fisher and X. Wang, *Adv. Sci.*, 2015, **2**, 1500120.

[246] Z. Wang, Y. Lu, Y. Yan, T. Y. P. Larissa, X. Zhang, D. Wuu, H. Zhang, Y. Yang and X. Wang, *Nano Energy*, 2016, **30**, 368-378.

[247] M. S. Xie, B. Y. Xia, Y. Li, Y. Yan, Y. Yang, Q. Sun, S. H. Chan, A. Fisher and X. Wang, *Energy Environ. Sci.*, 2016, **9**, 1687-1695.

[248] P. Xiao, X. Ge, H. Wang, Z. Liu, A. Fisher and X. Wang, *Adv. Funct. Mater.*, 2015, **25**, 1520-1526.

[249] P. Xiao, M. A. Sk, L. Thia, X. Ge, R. J. Lim, J.-Y. Wang, K. H. Lim and X. Wang, Energy *Environ. Sci.*, 2014, **7**, 2624-2629.

[250] Z. W. Seh, K. D. Fredrickson, B. Anasori, J. Kibsgaard, A. L. Strickler, M. R. Lukatskaya, Y. Gogotsi, T. F. Jaramillo and A. Vojvodic, *ACS Energy Lett.*, 2016, **1**, 589-594.

[251] C. Ling, L. Shi, Y. Ouyang, Q. Chen and J. Wang, *Adv. Sci.*, 2016, **3**, 1600180.

[252] C. E. Ren, K. B. Hatzell, M. Alhabeb, Z. Ling, K. A. Mahmoud and Y. Gogotsi, *J. Phys.* Chem. *Lett.*, 2015, **6**, 4026-4031.

[253] K. Rasool, K. A. Mahmoud, D. J. Johnson, M. Helal, G. R. Berdiyorov and Y. Gogotsi, *Sci. Rep.*, 2017, **7**, 1598.

[254] A. M. Jastrzebska, A. Szuplewska, T. Wojciechowski, M. Chudy, W. Ziemkowska, L. Chlubny, A. Rozmyslowska and A. Olszyna, *J. Hazard. Mater.*, 2017, **339**, 1-8.

[255] Q. Hu, D. Sun, Q. Wu, H. Wang, L. Wang, B. Liu, A. Zhou and J. He. *J. Phys. Chem. A.*, 2013, **117**, 14253-14260.

[256] R. Wu, H. Du, Z. Wang, M. Gao, H. Pan and Y. Liu. *J. Power Sources*, 2016, **327**, 519-525.

[257] A. Yadav, Alpa Dashora, N. Patel, A. Miotello, M. Press, D.C. Kothari. *Appl. Surf. Sci.*, 2016, **389**, 88-95.

[258] Y. Liu, H. Du, X. Zhang, Y. Yang, M. Gao and H. Pan. *Chem. Commun.*, 2016, **52**, 705-708.

[259] H. Fashandi, M. Dahlqvist, J. Lu, J. Palisaitis, S. I. Simak, I. A. Abrikosov, J. Rosen, L. Hultman, M. Andersson, A. Lloyd Spetz and P. Eklund, *Nat. Mater.*, 2017, **16**, 814-818.

[260] J. Wang, J. Tang, B. Ding, V. Malgras, Z. Chang, X. Hao, Y. Wang, H. Dou, X. Zhang and Y. Yamauchi, *Nat. Commun.*, 2017, **8**, 15717.

[261] Y. Dong, Z.-S. Wu, S. Zheng, X. Wang, J. Qin, S. Wang, X. Shi and X. Bao, *ACS Nano*, 2017, **11**, 4792-4800.

[262] X. Zhang, Z. Zhang, J. Li, X. Zhao, D. Wu and Z. Zhou, *J. Mater. Chem. A*, 2017, **5**, 12899-12903.

Table 1 Summary of specific capacitance and stability of MXene-based electrode materials for supercapacitors

Materials	Specific capacitance (scan rate)	Electrolyte	Stability capacity retention	Ref.
$Ti_3C_2T_x$	350 F cm^{-3} (1 A g^{-1})	1 M KOH	~100% (10,000 cycles)	2013[58]
d-Ti_3C_2	415 F cm^{-3} (5 A g^{-1})	1 M H_2SO_4	~100% (10,000 cycles)	2014[183]
Ti_3C_2	900 F cm^{-3}(2 mV s^{-1})	1 M H_2SO4	~100% (10,000 cycles)	2014[108]
$Ti_3C_2T_x$/PVA	530 F cm^{-3} (2 mV s^{-1})	1 M KOH	~100% (10,000 cycles)	2014[152]
$Ti_3C_2T_x$	51 F g^{-1} (1 A g^{-1})	30 wt % KOH	93% (6000 cycles)	2015[184]
$Ti_3C_2T_x$/CNT	350 F cm^{-3} (5 A g^{-1})	1 M MgSO4	~100% (10,000 cycles)	2015[160]
$Ti_3C_2T_x$/Ni-foam	499 F g^{-1} (2 mV s^{-1})	1 M H_2SO_4	~100% (10,000 cycles)	2015[191]
Ti_3C_2	117 F/g (2 mV s^{-1})	1 M KOH	97% (10,000 cycles)	2015[192]
Ti_3C_2/CNT	393 F cm^{-3}(5 mV s^{-1})	6 M KOH	100% (10,000 cycles)	2015[159]
$Ti_3C_2T_x$	357 F cm^{-3} (0.2 mA cm^{-2})	$Ti_3C_2T_x$	100% (10,000 cycles)	2016[189]
$Ti_3C_2T_x$ hydrogel	70 F g^{-1} (1 mV s^{-1})	1 M EMI-TFSI	80% (1,000 cycles)	2016[179]
$Ti_3C_2T_x$/CNT	85 F g^{-1} (2 mV s^{-1})	1 M EMI-TFSI	90% (1,000 cycles)	2016[161]
Ti_3C_2/TiO_2	143 F g^{-1} (5 mV s^{-1})	6 M KOH	92% (6,000 cycles)	2016[138]
Ti_3C_2	118 F g^{-1} (5 mV s^{-1})	6 M KOH	100% (5,000 cycles)	2016[182]
Ti_3C_2/MnO_2	377 mF cm^{-2} (5 mV s^{-1})	6 M KOH	95% (5,000 cycles)	2016[139]
Ti_3C_2/Ppy	406 F cm^{-3} (30 mV s^{-1})	0.5 M H_2SO_4	100% (20,000 cycles)	2016[156]
$Ti_3C_2T_x$/Ppy	1000 F cm^{-3} (5 mV s^{-1})	1 M H_2SO_4	92% (25,000 cycles)	2016[155]
Mo_2CT_x	700 F cm^{-3} (2 mV s^{-1})	1 M H_2SO_4	100% (10,000 cycles)	2016[118]
$Ti_3C_2T_x/MoO_3$	151 F g^{-1} (2 mV s^{-1})	1 M KOH	93.7% (8,000 cycles)	2016[142]
$Ti_3C_2T_x$	250 F cm^{-3} (10 mV s^{-1})	1 M H_2SO_4	100% (10,000 cycles)	2016[122]
Ti_3C_2/ NiAl-LDH	1061 F g^{-1} (1 A g^{-1})	6 M KOH	70% (4,000 cycles)	2016[145]
$Ti_3C_2T_x$/G	154.3 F g^{-1} (2 A g^{-1})	2 M KOH	85% (6,000 cycles)	2016[165]
Ti_3C_2/ZnO	120 F g^{-1} (2 mV s^{-1})	1 M KOH	85% (10,000 cycles)	2016[143]
$Ti_3C_2T_x$/G	216 F cm^{-3} (20 mV s^{-1})	PVA/H_3PO_4 gel	82% (2,500 cycles)	2017[39]
$Ti_3C_2T_x$/Li	892 F cm^{-3}(2 mV s^{-1})	1 M H_2SO_4	100% (10,000 cycles)	2017[193]
PANI@$TiO_2/Ti_3C_2T_x$	188 F g^{-1} (10 mV s^{-1})	1 M KOH	94% (8,000 cycles)	2017[186]
N-Ti_3C_2	266.5 F g^{-1} (5 mV s^{-1})	6 M KOH	86.4% (2,000 cycles)	2017[185]
$Ti_3C_2T_x$/rGO	1040 F cm^{-3} (2 mV s^{-1})	3 M H_2SO_4	100% (20,000 cycles)	2017[187]
$Ti_3C_2T_x$ hydrogel	1500 F cm^{-3} (2 mV s^{-1})	3 M H_2SO_4	90% (10,000 cycles)	2017[181]

Table 2 Summary of capacitive performance and cycling stability of MXene-based electrode materials for batteries.

Materials	Device	Role	Capacity (mAh g^{-1})	Cycling stability (mAh g^{-1})	Ref.
Ti_2C	LIBs	Cathode	225 (C/25)	70 (10 C, 200 cycles)	197
Ti_3C_2	LIBs	Anode	123.6 (1 C)	88 (3 C, 100 cycles)	110
Oxidized Ti_2C	LIBs	Anode	389 (0.1 A g^{-1})	280 (1 A g^{-1}, 1000 cycles)	204
Ti_3CNT_x	LIBs	Anode	343 (0.05 A g^{-1})	300 (0.5 A g^{-1}, 1000 cycles)	212
Nb_2CT_x/CNT	LIBs	Anode	780 (0.5 C)	430 (2.5 C, 300 cycles)	121
$Ti_3C_2T_x$/CNF	LIBs	Anode	320 (1 C)	97 (100 C, 2900 cycles)	167
$Ti_3C_2T_x/Co_3O_4$	LIBs	Anode	1200 (0.1 C)	410 (5 C, 150 cycles)	40
Ti_2CT_x/Cu_2O	LIBs	Anode	790 (0.01 A g^{-1})	143 (1 A g^{-1}, 200 cycles)	37
$Nb_4C_3T_x@Nb_2O_5$	LIBs	Anode	208 (0.25 C)	196 (0.25 C, 400 cycles)	38
Mo_2C/N-d-C	LIBs	Anode	744.6 (2 A g^{-1})	732.9 (2 A g^{-1}, 700 cycles)	168
$Ti_3C_2T_x$/CNT	LIBs	Anode	1250 (0.1 C)	500 (0.5 C, 100 cycles)	206
Sn-Ti_3C_2	LIBs	Anode	1375 (0.1 A g^{-1})	544 (1.75 C, 200 cycles)	126
$Ti_3C_2T_x$/Ag	LIBs	Anode	320 (1C)	310 (1 C, 5000 cycles)	36
$Ti_3C_2T_x/SnO_2$	LIBs	Anode	103 (0.1 A g^{-1})	360 (0.1 A g^{-1}, 200 cycles)	136
$Ti_3C_2T_x$/CNT	LIBs	Cathode	100 (0.1 C)	80 (1 C, 500 cycles)	211
Ti_3C_2	LSBs	Cathode	1291 (0.2 A g^{-1})	970 (0.2 A g^{-1}, 100 cycles)	218
Ti_2C/S	LSBs	Cathode	1200 (C/5)	960 (C/2, 400 cycles)	221
Ti_3C_2-CNT/S	LSBs	Cathode	1216 (C/20)	450 (C/2, 1200 cycles)	164
Ti_2C	NIBs	Cathode	90 (1 A g^{-1})	100 (0.6 A g^{-1}, 100 cycles)	226
Ti_3C_2/CNTs	NIBs	Anode	501 (0.02 A g^{-1})	175 (0.02 A g^{-1}, 100 cycles)	163
$Ti_3C_2T_x/MoS_2$	NIBs	Anode	392.6 (0.05 A g^{-1})	250.9 (0.1 A g^{-1}, 100 cycles)	146

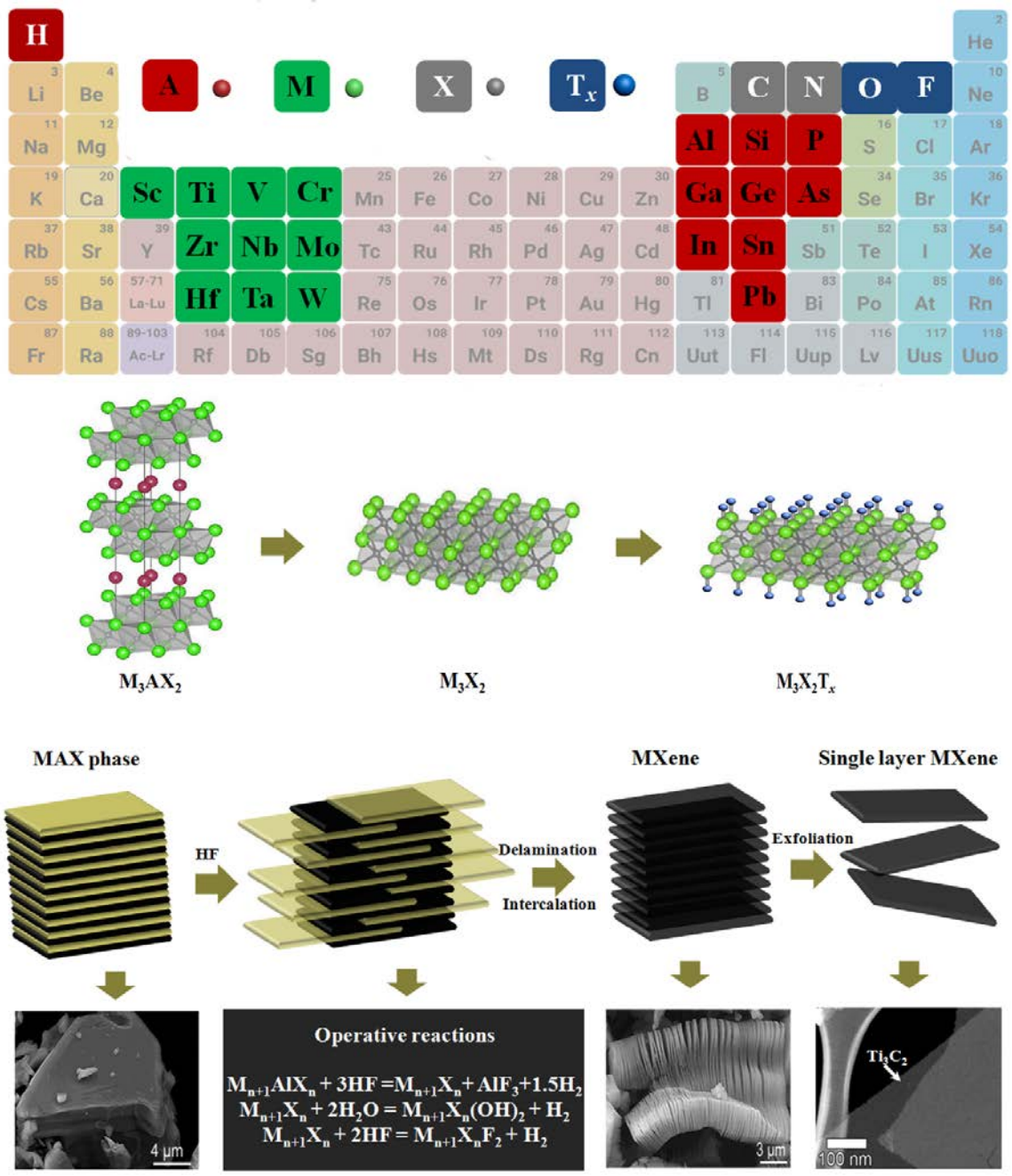

Figure 1. Illustration of the M_3AX_2, M_3X_2 and $M_3X_2T_x$ configurations, and schematic depicting the synthesis process of MXene using HF as the etchant. Adapted with permission from ref.[73, 106] Copyright © 2012 and 2016 American Chemical Society.

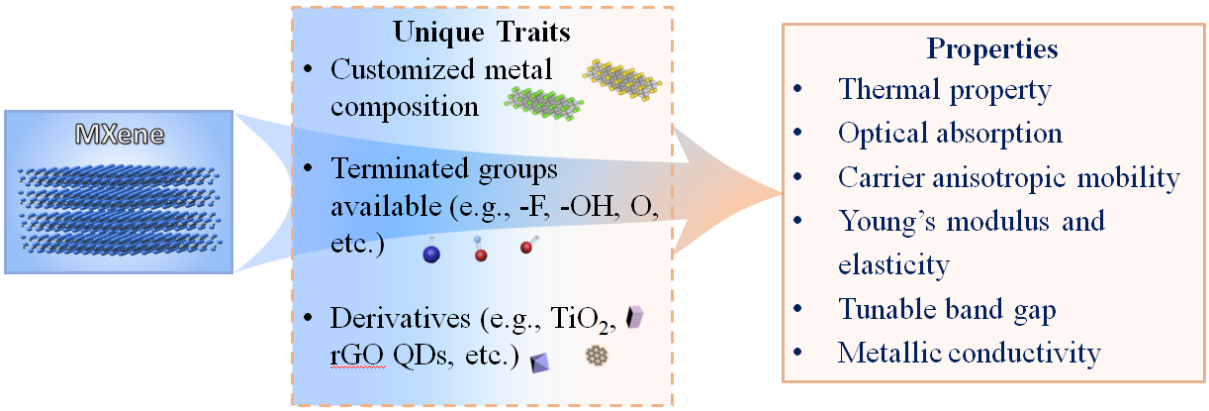

Figure 2. Schematic of the unique traits and properties of MXene.

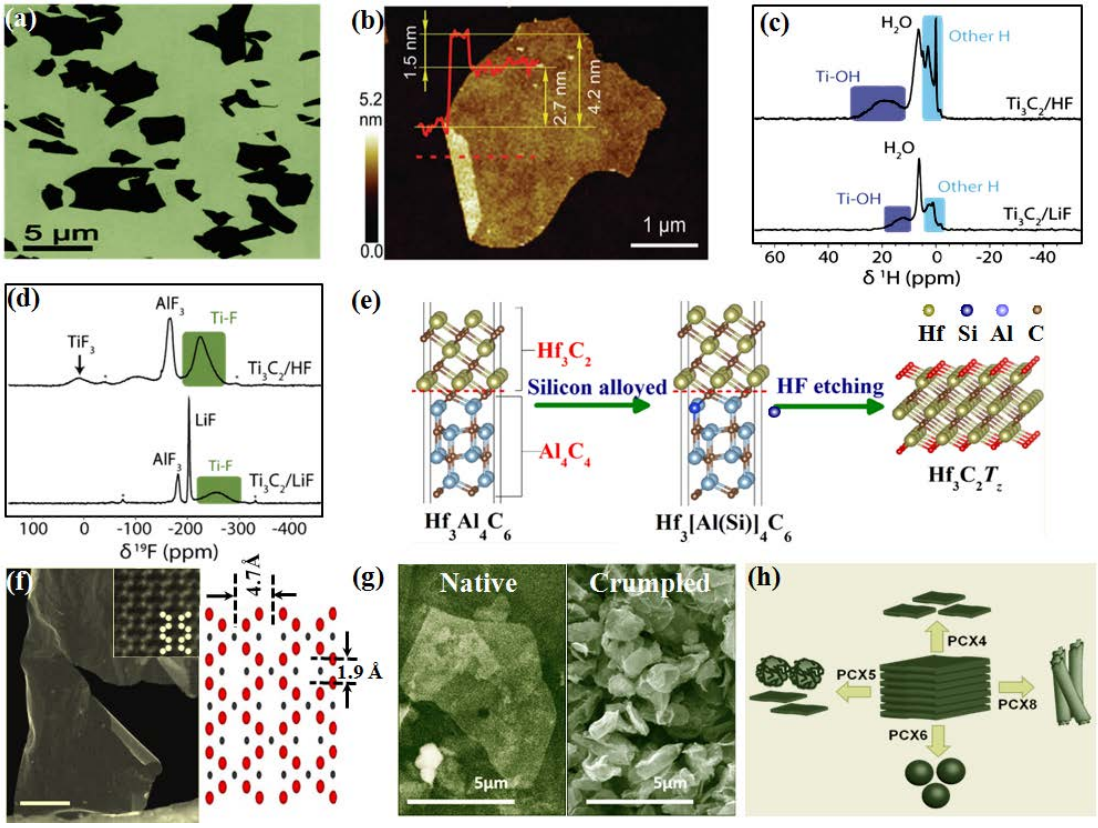

Figure 3. (a) SEM images of $Ti_3C_2T_x$ flakes. (b) AFM image of a folded $Ti_3C_2T_x$ flake. Adapted with permission from ref.[70] Copyright © 2016 Wiley-VCH Verlag GmbH & Co. KGaA, Weinheim. (c, d) ^1H and ^{19}F NMR (11.7 T) spectra of Ti_3C_2 MXene synthesized with HF and LiF-HCl recorded at 60 kHz MAS. (e) Schematic diagram showing the synthesis route of the $Hf_3C_2T_z$ MXene. Adapted with permission from ref.[32,113] Copyright © 2016 Royal Society of Chemistry. (f) HAADF-STEM of single $Mo_{1.33}C$ sheet with ordered divacancies and the ideal atomic structure from theoretically simulated parent MAX phase. Adapted with permission from ref.[115] Copyright © 2017 Nature publishing group. (g) SEM images of $Ti_3C_2T_x$ MXene nanosheets with native and crumpled morphology. Adapted with permission from ref.[116] Copyright © 2016 American Chemical Society. (h) Schematic illustration summarizing the synthesis of different morphologies of Ti_2C. Adapted with permission from ref.[117] Copyright © 2017 Wiley-VCH Verlag GmbH & Co. KGaA, Weinheim.

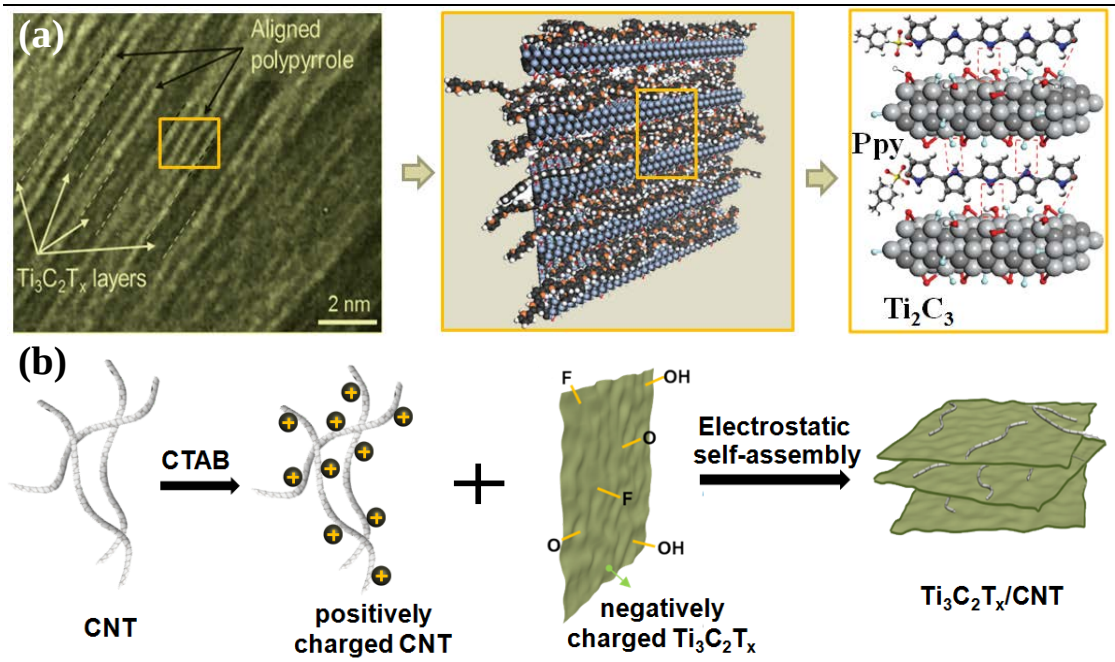

Figure 4. (a) The cross-sectional TEM image and schematic of aligned polypyrrole (Ppy) chains between MXene sheets. Adapted with permission from ref.[155, 156] Copyright © 2016 Wiley-VCH Verlag GmbH & Co. KGaA, Weinheim. (b) Schematic of the $Ti_3C_2T_x$/CNT composite preparation by self-assembly method. Adapted with permission from ref.[163] Copyright © 2016 Elsevier.

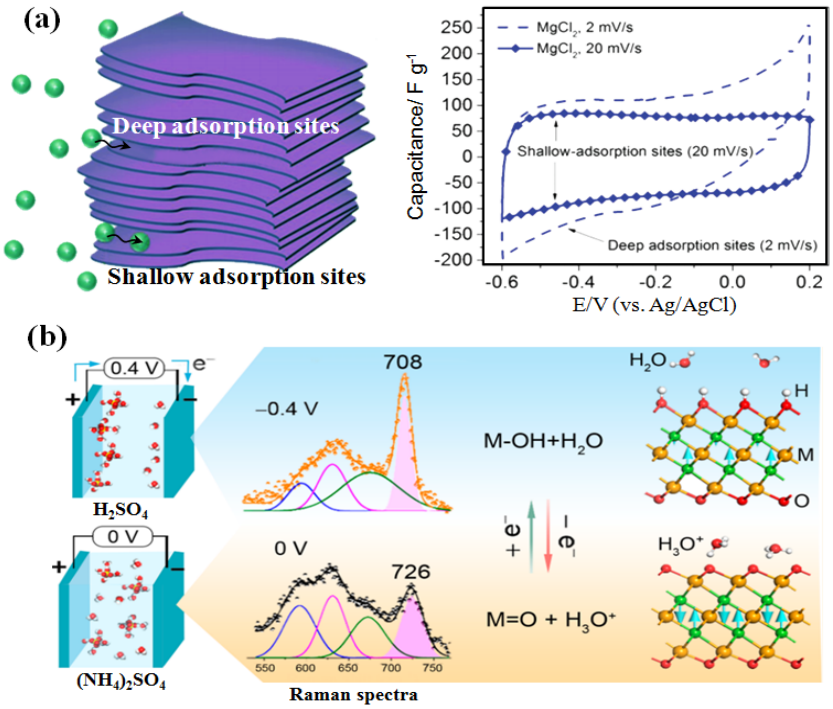

Figure 5. (a) Adsorption sites of multilayered $Ti_3C_2T_x$ particle and the corresponding capacitance of $Ti_3C_2T_x$/carbon black-PTFE laminate at scan rates of 2 mV s^{-1} and 20 mV s^{-1} in 1 M $MgCl_2$. Adapted with permission from ref.[176] Copyright © 2015 Wiley-VCH Verlag GmbH & Co. KGaA, Weinheim. (b) $Ti_3C_2T_x$-based electrode in H_2SO_4 and $(NH_4)_2SO_4$ electrolyte and the schematic illustration of reversible electrochemical transformation between M-O and M-OH. Adapted with permission from ref. [60] Copyright © 2016 American Chemical Society.

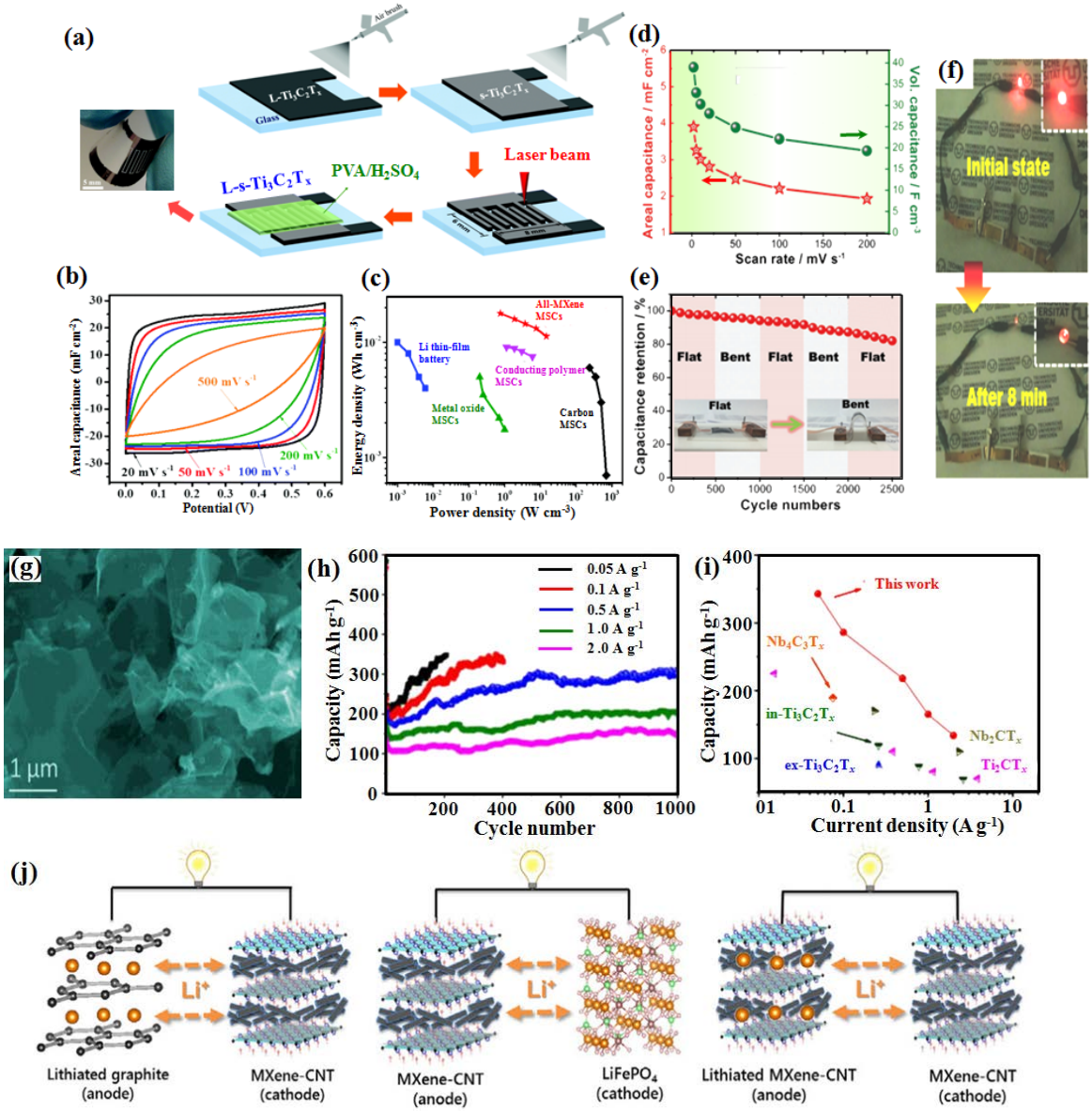

Figure 6. (a) Fabrication process of all-$Ti_3C_2T_x$ MSC; (b) Cyclic voltammetry curves of the *L-s*-$Ti_3C_2T_x$ MSC at different scan rates; (c) Ragone plot of the volumetric energy and power densities in different MSC. Adapted with permission from ref.[189] Copyright © 2016 Royal Society of Chemistry; (d) Areal capacitance and volumetric capacitance of MSCs at different scan rates; (e) Capacitance retention in the alternative flat and bent configurations after 2500 cycles at a scan rate of 200 mV s^{-1}, with the inset showing photographs of the microdevice in the flat and bent configurations; (f) Images show a LED powered using the three tandem ASSSs in winding and in plane. Adapted with permission from ref.[39] Copyright © 2017 Wiley-VCH Verlag GmbH & Co. KGaA, Weinheim. (g) SEM image of freeze-dried Ti_3CNT_x nanosheets; (h, i) Capacity comparison of freeze-dried Ti_3CNT_x to the literature. Adapted with

permission from ref. [212] Copyright © 2017 Elsevier. (j) Schematic of the Nb_2CT_x/CNT-based cell. Adapted with permission from ref. [156] Copyright © 2016 Elsevier.

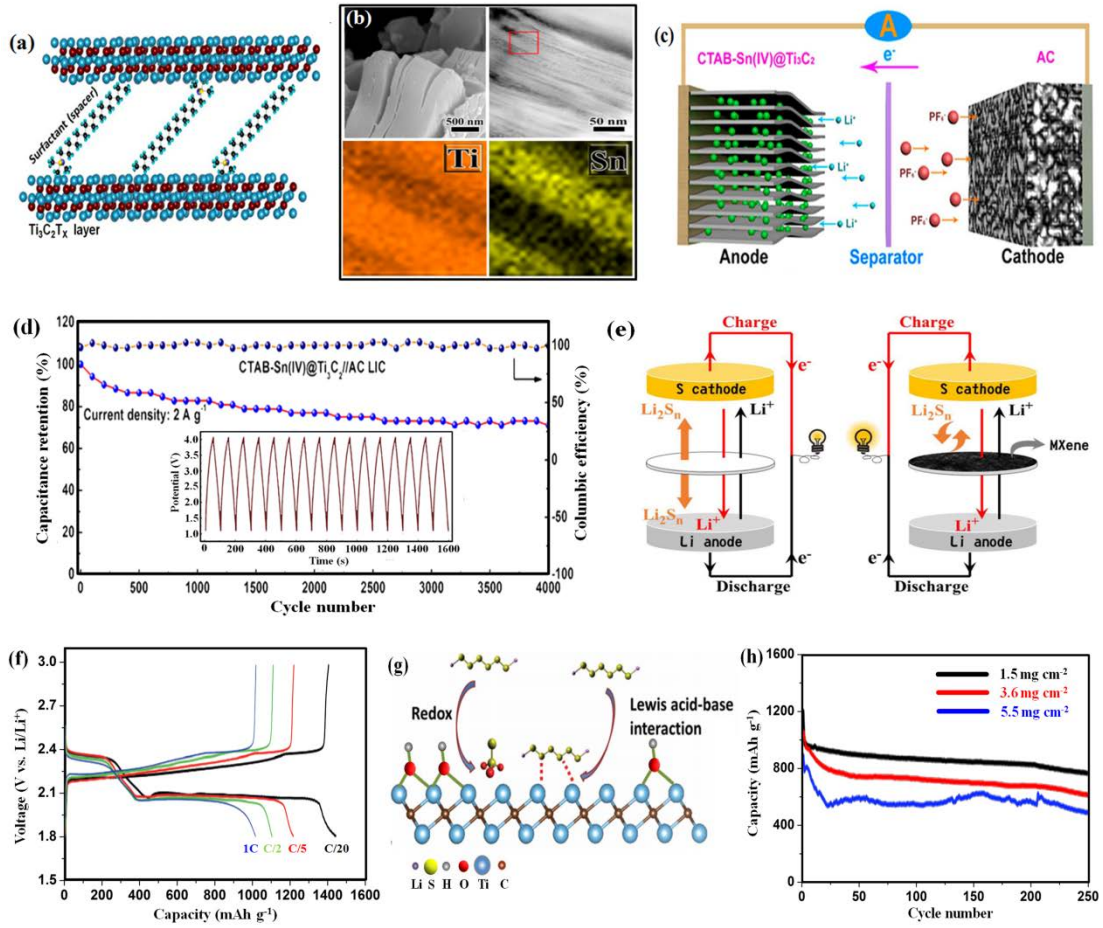

Figure 7. (a) Possible position of CTAB in the interlayer space of Ti_3C_2; (b) SEM, TEM and element mapping image of CTAB−Sn(IV)@Ti_3C_2; (c) The charging process; and (d) the charge−discharge curves of CTAB−Sn(IV)@Ti_3C_2//AC lithium ion capacitor at 2 A g^{-1}. Adapted with permission from ref.[125] Copyright © 2016 American Chemical Society. (e) Schematic configuration of the Li−S cells using polypropylene and MXene-polypropylene separators. Adapted with permission from ref.[220] Copyright © 2016 American Chemical Society. (f) Voltage profiles of 70wt% S/Ti_2C at various rates ranging from C/20 to 1C. Adapted with permission from ref.[221] Copyright © 2015 Wiley-VCH Verlag GmbH & Co. KGaA, Weinheim. (g) Schematic of the two-step interaction between hydroxyl-decorated MXene phase and polysulfides. (h) Long-term cycling performance of cells with 3.6 and 5.5 mg cm^{-2} sulfur loadings were examined at C/5. Adapted with permission from ref.[164] Copyright © 2017 Wiley-VCH Verlag GmbH & Co. KGaA, Weinheim.

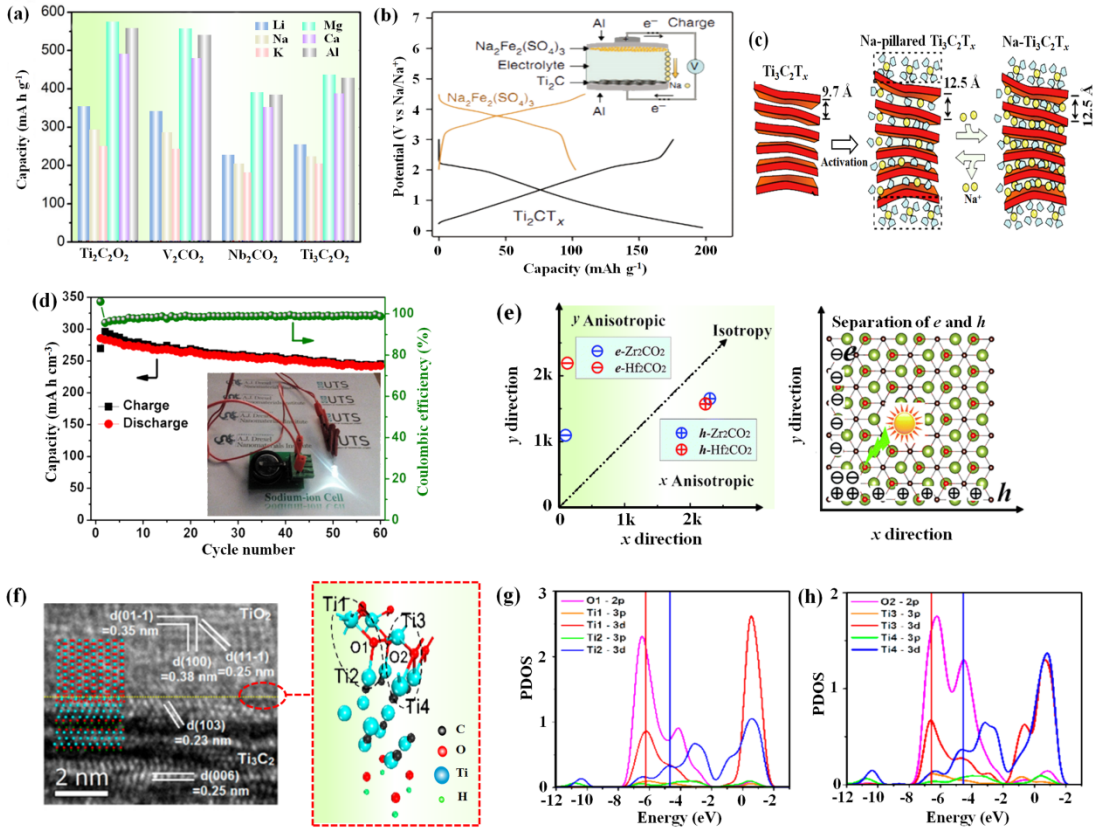

Figure 8. (a) Theoretical capacities on O-terminated MXene nanosheets. Adapted with permission from ref. [215] Copyright © 2016 American Chemical Society. (b) Charge/discharge curves of Ti_2CT_x and alluaudite $Na_2Fe_2(SO_4)_3$ versus Na/Na^+; the specific currents are 30 and 6 mA g^{-1}, respectively. The inset is a schematic illustration of the Ti_2CT_x-alluaudite $Na_2Fe_2(SO_4)_3$ full cell. Adapted with permission from ref.[226] Copyright © 2015 Nature Publishing. (c) Schematic illustration for the Na^+ insertion mechanism into $Ti_3C_2T_x$. Adapted with permission from ref.[225] Copyright © 2016 American Chemical Society. (d) The cycling performance at a current density of 50 mA $(g\text{-}Ti_3C_2T_x/CNT\text{-}SA)^{-1}$. The inset is the as-assembled full sodium-ion cell which can light up a LED. Adapted with permission from ref.[163] Copyright © 2016 Elsevier. (e) Carrier mobility of 2D Zr_2CO_2 and Hf_2CO_2 as a function of directions and schematic picture depicting the separation of photogenerated electron–hole pairs. Adapted with permission from ref.[59] Copyright © 2016 Royal Society of Chemistry. (f) SEM image of the interface structures and simulated interface structures of TiO_2/Ti_3C_2, and the partial density of states analyses of four kinds of Ti atom. (g, h) The partial density of states (PDOS) analysis of Ti1−O1−Ti2 and Ti3−O2−Ti4. Adapted with

permission from ref.[140] Copyright © 2016 American Chemical Society.

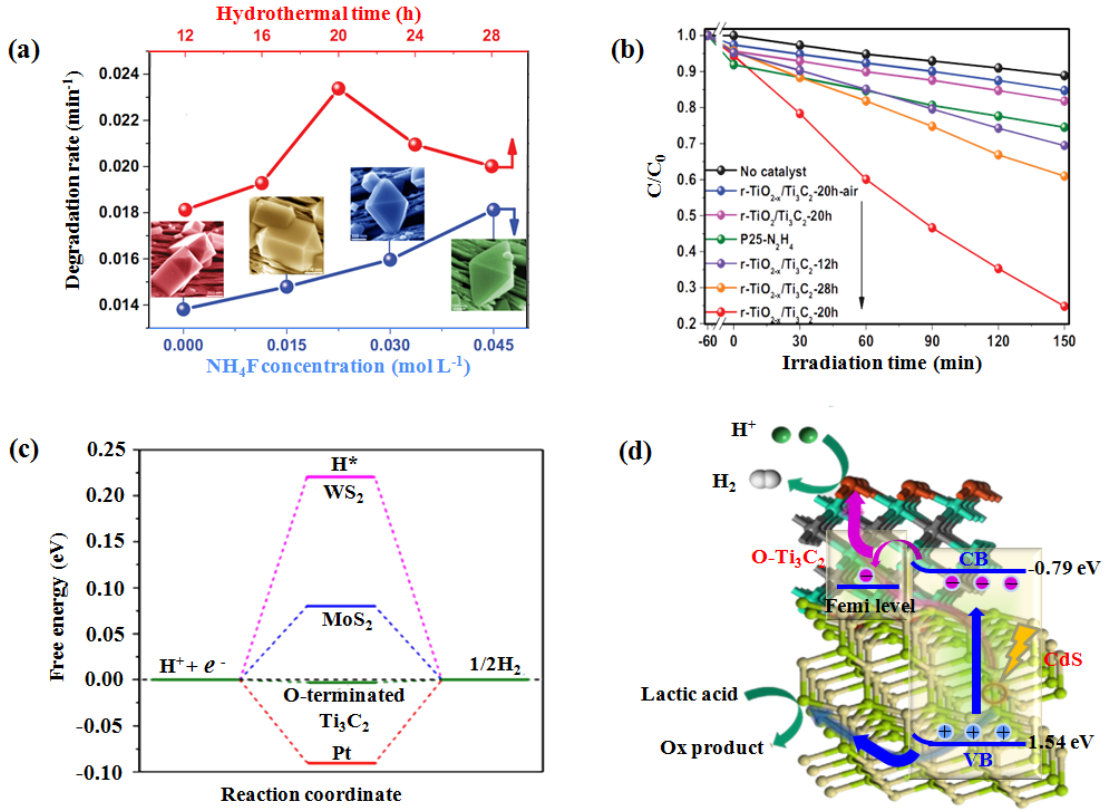

Figure 9. (a) The degradation rate constant of photocatalytic degradation of MO under ultraviolet light catalyzed by (111) r-TiO_2/Ti_3C_2 prepared under different condition. (b) Photo-generated carrier transfer process and photocatalytic degradation of MB over (111) r-TiO_{2-x}/Ti_3C_2 under visible light irradiation. Adapted with permission from ref.[92] Copyright © 2017 Elsevier. (c) Comparison of calculated free-energy diagram of HER for O-terminated Ti_3C_2, Pt, MoS_2, and WS_2. (d) Proposed mechanism for photocatalytic H_2 production in CdS/Ti_3C_2 system under visible-light irradiation. Adapted with permission from ref.[41] Copyright © 2017 Nature publishing.

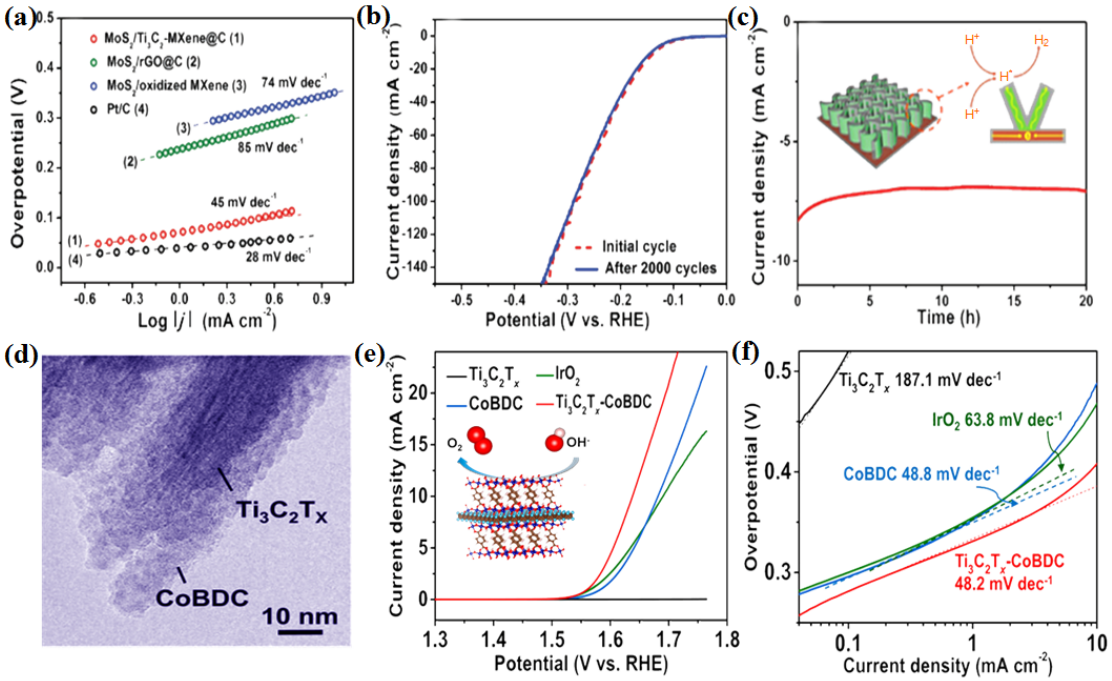

Figure 10 (a) Tafel plots of various catalysts. (b) Polarization curves after continuous potential sweeps of 2000 cycles at 50 mV s^{-1} over the MoS_2/Ti_3C_2-MXene@C catalyst. (c) Time-dependent current density curves at η = 130 mV for the MoS_2/Ti_3C_2-MXene@C catalyst. Adapted with permission from ref.[147] Copyright © 2017 Wiley-VCH Verlag GmbH & Co. KGaA, Weinheim. (d) Cross-sectional view of a few stacked $Ti_3C_2T_x$/CoBDC hybrid nanosheets. (e) Oxygen evolution reaction polarization curves of different catalysts and the schematic illustration of the $Ti_3C_2T_x$/CoBDC hybrid in the inset. (f) Tafel plots of various electrodes. Adapted with permission from ref.[60] Copyright © 2017 American Chemical Society.

Table of Contents Entry

Clay-inspired MXene-based electrochemical devices and photo-electrocatalyst: State-of-the-Art progresses and challenges

By *Hou Wang, Yan Wu, Xingzhong Yuan, Guangming Zeng, Jin Zhou, Xin Wang,* Jia Wei Chew **

Keywords: MXene, supercapacitor, battery, photocatalyst, and electrocatalyst

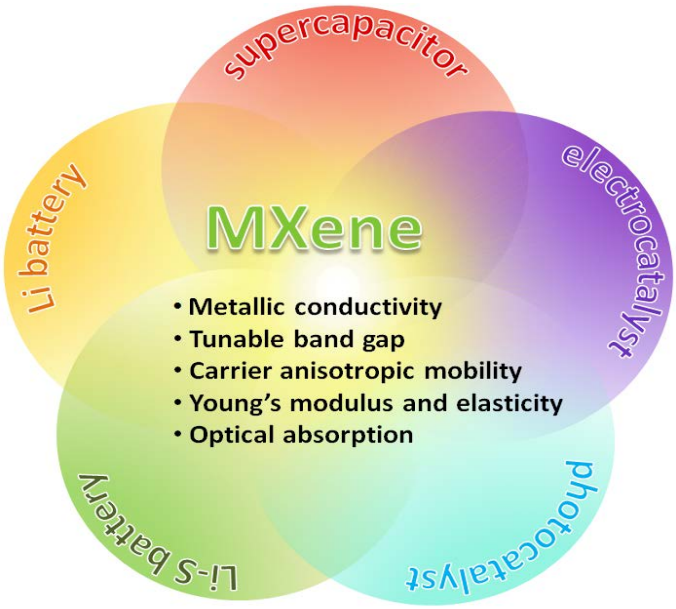

This review provides an overview in the fundamental properties and synthesis routes of pure MXene, functionalized MXene and their hybrids, highlights the state-of-the-art progresses of MXene-based applications with respect to supercapacitors, batteries, electrocatalysis and photocatalysis, and presents the challenges and prospects in the burgeoning field.

Author Photographs

Hou Wang received his PhD degree at Hunan University in 2016. At present, he is working as a postdoctoral researcher at Nanyang Technological University. His research focuses on the synthesis and application of advanced nanomaterials. He has published 60 peer-reviewed articles with a total citation of more than 1500 and H-index of 22.

Xin Wang has been with the School of Chemical and Biomedical Engineering since 2005, and is currently a Professor and Associate Dean (research) of the College of Engineering. He received his Bachelor and Master degrees in Chemical Engineering from Zhejiang University, Ph.D. degree from the Hong Kong University of Science and Technology. His research interests include electrochemistry, electrochemical technologies for energy conversion. He has done significant research work in his research areas and published over 160 peer-reviewed journal papers, with total citation over 12,000 and H-index of 61. He is a Fellow of the Royal Society of Chemistry (FRSC).

Jia Wei Chew received her PhD degree in Chemical Engineering (2011) from University of Colorado at Boulder. She joined the School of Chemical & Biomedical Engineering at Nanyang Technological University as an Assistant Professor in 2013. Her main research interests include membrane technology and particle technology. She has published over 80 peer-reviewed research articles with a total citation of more than 1,000 and H-index of 17.